



저작자표시-비영리-변경금지 2.0 대한민국

이용자는 아래의 조건을 따르는 경우에 한하여 자유롭게

- 이 저작물을 복제, 배포, 전송, 전시, 공연 및 방송할 수 있습니다.

다음과 같은 조건을 따라야 합니다:



저작자표시. 귀하는 원저작자를 표시하여야 합니다.



비영리. 귀하는 이 저작물을 영리 목적으로 이용할 수 없습니다.



변경금지. 귀하는 이 저작물을 개작, 변형 또는 가공할 수 없습니다.

- 귀하는, 이 저작물의 재이용이나 배포의 경우, 이 저작물에 적용된 이용허락조건을 명확하게 나타내어야 합니다.
- 저작권자로부터 별도의 허가를 받으면 이러한 조건들은 적용되지 않습니다.

저작권법에 따른 이용자의 권리는 위의 내용에 의하여 영향을 받지 않습니다.

이것은 [이용허락규약\(Legal Code\)](#)을 이해하기 쉽게 요약한 것입니다.

[Disclaimer](#)

Ph. D. DISSERTATION

Experimental Investigation of
Concentration Boundary Layer
Induced by Permselective Ion Transport

선택적 이온전달현상에 의해 유도된
농도경계층의 실험적 검증

BY
JUNSUK KIM

FEBRUARY 2019

DEPARTMENT OF
ELECTRICAL AND COMPUTER ENGINEERING
COLLEGE OF ENGINEERING
SEOUL NATIONAL UNIVERSITY

Experimental Investigation of
Concentration Boundary Layer
Induced by Permselective Ion Transport

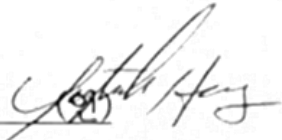
지도 교수 김 성 재

이 논문을 공학박사 학위논문으로 제출함
2019 년 2 월

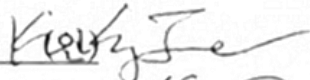
서울대학교 대학원
전기정보공학부
김 준 석

김준석의 공학박사 학위논문을 인준함
2019 년 2 월

위 원 장 _____ 홍 용 택

(인) 

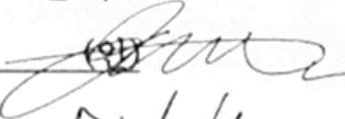
부위원장 _____ 김 성 재

(인) 

위 원 _____ 김 호 영

(인) 

위 원 _____ 이 종 호

(인) 

위 원 _____ 박 노 균

(인) 

Abstract

Experimental Investigation of Concentration Boundary Layer Induced by Permselective Ion Transport

JUNSUK KIM

DEPARTMENT OF
ELECTRICAL AND COMPUTER ENGINEERING
COLLEGE OF ENGINEERING
SEOUL NATIONAL UNIVERSITY

In this thesis, physical properties of concentration boundary layer induced by permselective ion transportation was discussed. Investigating concentration boundary layer is an important subject since the layer is one of the starting point of causing various interesting physical phenomena. If we properly obtain the concentration boundary layer profile, not only does it help exploring unique phenomena arising from the permselective ion transportation but also it can support ground data when conceiving engineering applications. However, modeling electrokinetic transport phenomena is highly complex because it requires simultaneous solution of continuity equation, Navier-Stokes equation, Nernst-Planck equation, Poisson equation. Also, boundary conditions should be considered too such as device geometry, surface potential, porosity of the nanoporous membrane *etc.* Due to these diversity and complexity, answering the concentration

boundary layer profile exactly still remained as an enigma. Acquiring experimental solutions are also a complex problem because direct measurement of concentration profiles is realistically unfeasible.

To expand the scientific understanding on permselective ion transportation, the thesis focused on the role of concentration boundary layer where microchannel was combined with nanoporous membrane. Concentration boundary layer was mainly induced by permselective ion transportation with its mechanism divided into two parts; electromigratory flux and diffusive flux. So, the thesis was divided into two parts which had background physics of ion concentration polarization (chapter 2, 3 & 5) and diffusiophoresis (chapter 4), respectively.

First in chapter 2, an air valve using Young-Laplace equation was conceived for the exact electrokinetic measurement along with convenient experiments. The new structural components of bifurcated side-microchannels connected to the main microchannel was proposed, which allowed to reduce the time needed for initial filling and flushing the device with sample. The formation of virtual valves due to Laplace pressure developed at liquid/air/hydrophobic solid interfaces prevented the leakage of a liquid. The air valve structure enabled exact electrokinetic responses in comparison to the conventional 1-D micro/nanofluidic device while saving times of filling and flushing in the microchannel of the conventional device.

Secondly in chapter 3, parallel formation of nanoporous membrane with the microchannel which had the effect of enhancing surface conduction was proposed. This geometry lead to the alternation ionic transportation mechanism from electroosmotic flow to surface conduction. The change of mechanism gave a unique property of stabilizing concentration boundary layer propagation even at high concentration electrolyte due to newly formed bifurcated current path. Also,

non-destructive cellular preconcentrator was demonstrated as an engineering application.

Thirdly in chapter 4, experimental investigations on the exclusion zone formation near the surface of an ion exchange medium in the presence of a steady channel flow were discussed. The exclusion zone was formed by diffusive flux of ions transporting into the nanoporous membrane. Exchange of cations at the Nafion/liquid interface created the concentration gradient of the ions near the side walls, which then formed an exclusion zone of suspended particles. Concentration boundary layer was characterized by Sherwood number which is a non-dimensional number. Different types of charged particles were tested to visualize exclusion zones under different conditions. Then the formation of exclusion zone in the channel flow was used as a method for water cleaning.

Finally in chapter 5, spatiotemporal concentration profile of diffusion-convection layer during ion concentration polarization process had been measured through microelectrodes to investigate the concentration profile directly. Au microelectrodes arrays fabricated by conventional lift-off process enabled measuring the local potentials of the microchannel. Traditional diffusion-convection layer showed linear concentration profile. However, the measured data indicated the existence of near plateau concentration distribution over the diffusion-convection layer in a microfluidic environment. Also, even though the plateau concentration region had rather higher concentration compare to ion depletion zone, it also acted as a virtual boundary of physical properties similar to ion depletion zone.

In this thesis, various experimental methods were adopted to elucidate the properties of concentration boundary layer in specific conditions. Concentration

boundary layer induced by permselective ion transportation was explored with two physical phenomena; ion concentration polarization and diffusiophoresis. Analytical approach based on experimental results was given with practical devices simultaneously. This work would expanded the scientific understandings on concentration boundary layer induced by permselective ion transportation.

Keywords: Micro/Nanofluid, Electrokinetics, Permselective Ion Transport, Ion Concentration Polarization, Diffusiophoresis, Preconcentration

Student Number: 2014-22550

Contents

Abstract	i
Contents	v
List of Figures	ix
List of Tables	x v
Chapter 1.Introduction	1
1.1 Permselective ion transport	1
1.2 Permselective ionic flux: migration-diffusion equation	3
1.3 Ion concentration polarization (ICP)	4
1.4 Diffusiophoresis	6
1.5 Thesis objective	8
1.6 Thesis outline	9
Chapter 2. Pseudo 1-D Micro/Nanofluidic Device for Exact Electrokinetic Responses	12
2.1 Introduction	12
2.2 The operation principle of the air valve	14
2.3 Experimental setups	18
2.4. Results and discussion.....	19
2.4.1 The flow tracking with opening and closing the air valve.....	19
2.4.2 The formations of the depletion boundary with opening and closing the air valve	21
2.4.3 Current-voltage responses with opening and closing the air valve	22
2.5. Conclusions	24

Chapter 3. Ion Concentration Polarization by Bifurcated Current Path

.....	26
3.1 Introduction	26
3.2 Experimental setups	28
3.3 Results and discussion.....	31
3.3.1 The characterization of bifurcated current path with equivalent circuit	31
3.3.2 The conductance measurement between a nanoporous membrane and the electrolyte solution inside a microchannel	33
3.3.3 The propagation of ICP layer upon bifurcated current path	35
3.3.4 I-t responses upon bifurcated current path	38
3.3.5 Non-destructive cellular preconcentrator	41
3.4. Conclusions	46

Chapter 4. Diffusiophoretic Exclusion of Colloidal Particles for

Continuous Water Purification.....	47
4.1 Introduction	47
4.2 Experimental setups	50
4.3 Results and discussion.....	52
4.3.1 Concept of micro/nanofluidic water purification	52
4.3.2 Boundary layer analysis	54
4.3.3 Continuous diffusiophoretic exclusion of colloidal particles	60
4.3.4 Long-time ion exchange to obtain actual sustainable time.....	65
4.4. Conclusions	67

Chapter 5. Experimental Investigation on Spatiotemporal

Concentration Profile of the Ion Concentration Polarization

Layer	68
5.1 Introduction	68
5.2 Experimental setups	72
5.2.1 Device Fabrication.....	72
5.2.2 Device operation.....	74
5.2.3 In situ concentration measurement	76
5.3 Results and discussion.....	77
5.3.1 Unexpected plateau concentration region.....	77
5.3.2 Experimental parameter sweep.....	80
5.3.2.1 Influence of fluorescent dye on plateau concentration	80
5.3.2.2 Bulk concentration vs. plateau concentration (%)	82
5.3.2.3 Influence of initial volumetric flow on plateau concentration	84
5.3.2.4 Rightness of <i>In situ</i> concentration measurement with Au microelectrodes	86
5.4. Conclusions	87
Chapter 6. Conclusions	88
Appendix	91
A. Pathogen preparation	91
B. Acid resistance assay for each pathogen	92
C. Fully-coupled model for ion concentration boundary layer by ion exchange	94

D. Boundary conditions for 2D fully-coupled model.....	97
Reference	98
Abstract in Korean (국문요약).....	105

List of Figures

Figure 1.1. The schematic figure of (a) non EDL overlap at microchannel (b) EDL overlap at nanochannel. Not to scale.....	2
Figure 1.2. The schematic figure on principle of ion concentration polarization (ICP) in the early model. N^+ and N^- are the number flux of cation and anion, respectively. ' <i>diff</i> ' represents diffusion.....	5
Figure 1.3. The schematic figure on principle of diffusiophoresis (chemiphoresis + induced electrophoresis).....	7
Figure 2.1. (a) Snapshot and (b) microscopic view of the fabricated pseudo 1-D ICP device. The sequences of operating air valve structures (c) Step 1: Flushing and (d) Step 2: Air cutting. The microscopic images of the meniscus at the air valve and its force balances (e) with and (f) without applied voltage. Here θ_1 and θ_2 were $\pi -$ (meniscus contact angle at the side PDMS wall without applied voltage) and $\pi -$ (meniscus contact angle at the side PDMS wall with 100 V applied voltage), respectively.....	17
Figure 2.2. The movement of fluorescent microparticles and dyes at the applied voltage of 10 V with (a) the opening the air valve and (b) closing the air valve. In each figure, the depletion boundaries were denoted as two opposite white arrows.	20

Figure 2.3. The propagation of the ion depletion zone in three different types of device. (a) Schematic diagrams of each device, (b) experimental results. The depletion boundaries were denoted as two opposite white arrows.....21

Figure 2.4 The current-voltage responses measured by experiments for three different types of device.23

Figure 2.5. Comparison of repeatability and preprocess time of three different types of device. Proposed Air valve 1-D ICP device had high repeatability and short preprocess time.....25

Figure 3.1. (a) Snapshot and microscopic view ((A) in red box) of the fabricated non-destructive cellular preconcentrator. L was the length of protruded nanoporous membrane from the main microchannel. Schematics of (b) top and (c) side view of the proposed devices with equivalent electrical resistors (not to scale).....32

Figure 3.2. Side schematic view of (a) simple straight microchannel device and (b) the device with patterned nanoporous membrane at the bottom. (c) Calculated ionic conductance of microchannel and nanoporous membrane..... 34

Figure 3.3. Time-revolving snapshots of propagating ion depletion zone (or ICP layer) at each concentrations with the applied voltage of 50 V; (a) Dilute limit (1 mM), (b) condensed limit (1 M) and (c) intermediate (31.6 mM). The schematic connections with the equivalent circuit were also given below each figures (not to scale). Red line indicated the dominant current paths.....37

Figure 3.4. Current-time responses of (a) $0.01 \times$ PBS media (~ 1.5 mM; dilute limit) and (b) $1 \times$ PBS media (~ 150 mM; condensed limit) with the various protruded length. Each figures had an inset of microscopic views in the case of $L = 3000$ μm . Capital letters indicated the time at which the snapshot were taken.40

Figure 3.5. Time-revolving snapshots of RBC preconcentration with the devices of protruded membrane length (a) $L = 1000$ μm and (b) $L = 6500$ μm . The amplification ratio of RBCs were ~ 40 fold in (b), while most of RBCs were destroyed in (a). In terms of the current path, the schematic diagrams of developed ion depletion zone at $t = 50$ sec for each cases were depicted in (c) and (d) (not to scale).45

Figure 4.1. (a) The schematic diagram of natural ion depletion mechanism around nanoporous medium. This diagram is conceptual schematic to understand ion exchange and ion depletion process. (b) Schematic diagram for micro/nanofluidic device utilizing diffusiophoretic exclusion of colloidal particles induced by concentration gradient inside ion concentration boundary layer. The arrows on colloidal particle denote velocity components; \mathbf{U}_{DP} is the diffusiophoretic velocity, \mathbf{U}_{conv} is the convective drag by ambient flow of colloidal suspension and \mathbf{U}_{net} is the net velocity of the colloidal particle. (c) Photo of assembled device and (d) the microscopic image of it.53

Figure 4.2. Exclusion layer depending on Sh . (b) Normalized concentration of Na^+ at outlet as a function of Sh . Solid line was the theoretical prediction by the boundary layer analysis and symbols were the experimental results as labeled. (c) The prediction of out-stream pH as a function of Sh (Inset: Experimentally measured out-stream pH).59

Figure 4.3. Diffusiophoretic exclusion layer of artificial microsphere (1 μm polystyrene) and pathogens (*E. coli* and *S. typhimurium*) with $Sh = 10$ (a) and $Sh = 0.1$ (b) respectively.64

Figure 4.4. (a) Microscopic images showing decrement of pathogen fluorescent signal with low pH. (b) % survival of pathogen under various pH obtained from acid resistance assay.64

Figure 4.5. Long-time operation on micro/nanofluidic ion exchange device. (a) Time-revolving snapshots of exclusion layer and (b) the thickness of exclusion layer as a function of time.66

Figure 5.1. Schematic diagrams of the concentration profile of ICP layer. (a) Initial model of ICP layer with diffusion and drift considered. (b) Non-linear electrokinetic fluid slip induced vortex was added to (a). (c) Multiple vortex caused by primary vortex was added to (b). (d) Proposed model including plateau concentration next to diffusion layer. 71

Figure 5.2. (a) Snapshot of the fabricated device containing Au μ -electrodes. The device was fabricated with conventional soft lithography method and lift-off process (b) 3-D schematic of the device showing the applied potential of each reservoirs and Au μ -electrodes measure the local potential. (c) Schematic figure of operating platform with microscopic view of the fabricated device. 75

Figure 5.3. (a) Microscopic view of time-evolving snapshots of the main microchannel with 10 mM KCl (c_0) as background electrolyte. Preconcentrated fluorescent dye were being propagated toward the anode. The region between two measured electrodes were indicated as red (c_{13}), yellow (c_{35}) and green (c_{57}) rectangles. Also, plateau concentration region was indicated as sky blue arrow. (b) Corresponding local average concentration vs. time responses of c_{13} , c_{35} and c_{57} . Each region reached plateau concentration ($\sim 0.6 c_0$) when the propagating fluorescent dye reached the left side of rectangle, respectively. 79

Figure 5.4. Local average concentration vs. time responses without fluorescent dye. After each region reached plateau concentration ($\sim 0.6 c_0$) the local average concentration was fixed. All seven μ -electrodes were used in this experiment. 81

Figure 5.5. (a) Initial bulk concentration vs. percentage of plateau concentration to bulk concentration ($\sim 0.6 c_0$). The plateau concentration phenomenon occurred at every concentration. (b) Local average concentration vs. time responses of two different bulk concentration 0.185 mM and 1.03 mM.83

Figure 5.6. Unstable measured data at high bulk concentration ($c_0 = 20$ mM) due to unstable ion depletion zone at electro-osmotic instability regime. (a) Unstable current-time responses and (b) unstable voltage difference between electrodes hindered the measurement of local average concentration.....83

Figure 5.7. Local average concentration vs. time responses (a) without initial volumetric flow and (b) with initial volumetric flow. The percentages of plateau concentrations to bulk concentration were similar.85

Appendix Figure D.1. Graphical representation of boundary conditions.....97

List of Tables

Appendix Table A.1. Sequences of synthesized oligonucleotides.	93
--	----

Chapter 1. Introduction

1.1 Permselective ion transport

Permselective ion transport is a preferential permeation of certain ionic species through ion exchange membrane. The free ions in the solution are either attracted to or repelled from a charged surface depending on the sign of the surface charges. Such a redistribution of free ions in the solution together with the surface ions give rise to what are known as electric double layers (EDL)[1]. Debye length, κ^{-1} is a measure of the electric double layer thickness, and is a property of the electrolyte solution which is defined as

$$\kappa^{-1} = \left(\frac{\varepsilon k_B T}{2e^2 z^2 n_\infty} \right)^{1/2} \quad (1.1)$$

Here, ε is dielectric permittivity of the solvent, k_B is Boltzmann constant, T is absolute temperature, e is elementary charge, z is the ionic valence, and bulk concentration n_∞ [1].

As equation 1.1 implies, the Debye length depends on ionic concentration and can vary from less than 1 nm at high ionic strength to a few tens of nanometers at low ionic strength. If the channel's dimension is larger than the Debye length, redistribution of counter ions compensate the channel's surface potential. Redistribution of ions leads the channel's potential to zero as shown in Figure 1.1(a). If the channel dimension becomes smaller and is comparable to the Debye length, overlap of EDL occurs. The mobile counter ions cannot compensate all the surface potential of the channel. Electric potential at the channel's center doesn't reach zero as shown in Figure 1.1(b). Due to this non-zero potential, electrical repulsion hinders transportation of co-ions through the channel while counter ions

can easily pass through the channel. The ratio between Debye length and the channel dimension is a critical parameter for permselective ion transportation since the overlap of EDL is a prerequisite condition. This phenomenon generally occurs at nanochannel or nanoporous membrane. Also, most substances' surface potential are negative (e.g. Silicon, Glass, Nafion)[2, 3] acting as a cation-selective channel. Therefore, cation-selective ion transportation will be dominantly covered in this thesis.

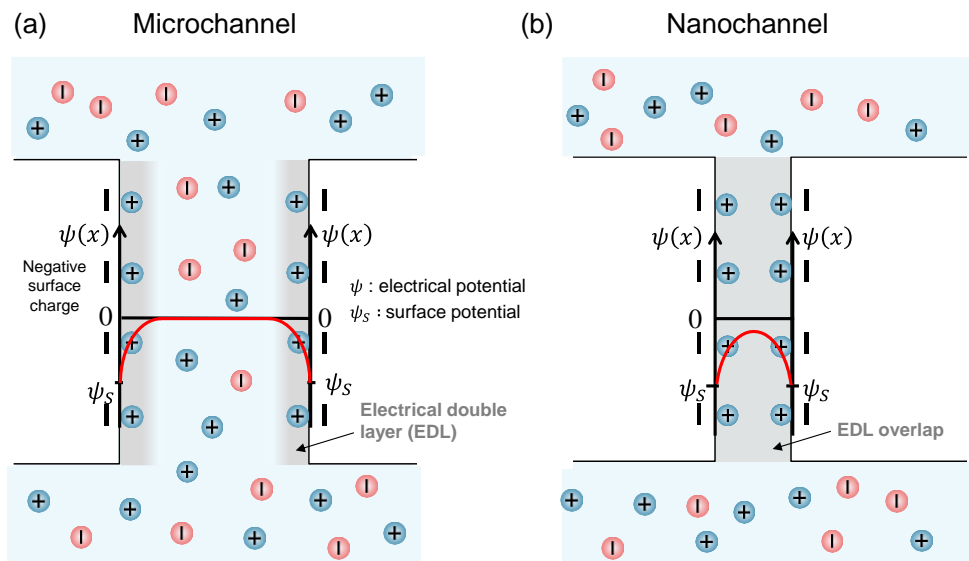


Figure 1.1. The schematic figure of (a) non EDL overlap at microchannel (b) EDL overlap at nanochannel. Not to scale.

1.2 Permselective ionic flux: migration-diffusion equation

Over the past decades, permselective ion transportation had drawn significant attentions in the field of not only biomedical[4] and environmental applications[5] but also the fundamental researches of electrokinetic theory[6-8]. The experimental exploration of permselective ion transportation was accelerated with the advent of nanoporous membrane and development of sophisticated fabrication methods for nanochannel[7]. When system was composed of microchannel combined with nanochannel, unique property arose not only inside the nanochannel but also at the junction of nanochannel and microchannel. This was due to the influence of permselective ion transportation on bulk electrolyte concentration. At the microchannel, the interests were the movement or mass transfer of the anions and the cations as well as the bulk concentration boundary. The permselective ionic flux (\mathbf{j}) of the i^{th} species was given by

$$\mathbf{j}_i = \frac{z_i}{|z_i|} \mu_i c_i \mathbf{E} - D_i \nabla c_i \quad (1.2)$$

where subscript ‘ i ’ represents i^{th} species, μ the electrophoretic mobility, c the concentration, \mathbf{E} the electric field, and D the diffusivity[1].

The first term on the right-hand side represented the contribution of electromigratory flux and the second term was due to the diffusive flux. The change of concentration affected all the physical parameters inside the system such as electric field, ionic flux, flow field, movement of particles, and so on.

Many research groups had utilized various concentration devices such as isoelectric focusing[9], capillary electrophoresis[10], electrokinetic trapping[11], field amplification stacking[12], isotachopheresis[13], affinity-based extraction[14]

and membrane filtration[15]. Among these various techniques, the thesis focused on the phenomena called ion concentration polarization (ICP) and diffusiophoresis, which utilized permselective ion transportation for the formation of concentration boundary layer.

1.3 Ion concentration polarization (ICP)

Among many permselective ion transportation related phenomena, ICP was considered as one of the most unique phenomenon utilizing electromigratory flux, since it had numerous exciting features in terms of nanoscale electrokinetics and the great applicability for the engineering fields that required the proficient manipulation of ions. ICP is the generation of a steep concentration gradient between the anodic/cathodic side of a nanoporous membrane (or nanochannel) under dc bias[16]. The essential mechanism of ICP is that only counter-ions can pass through a charged nanoporous membrane under dc bias[17, 18]. This results to the imbalance of ion concentrations at anodic and cathodic side of the membrane. The regions with low concentration at anodic side and high concentration at cathodic side are called an ion depletion zone and an ion enrichment zone, respectively[17, 18] as shown in Figure 1.2.

Micro/nanofluidic preconcentration device based on ICP was firstly reported in 2005, showing a factor up to a million-fold and easy operation[19]. The ion depletion zone contained various fundamental issues such as instability[20], overlimiting current[21], and nonlinear electrokinetic flow[22]. One of ion depletion zone's important property is locally amplified electric field and flow caused by high electrical resistance[22]. Although considerable progresses have

been made towards the understanding of ICP, the mechanism of concentration boundary layer formed by ICP is still rarely known.

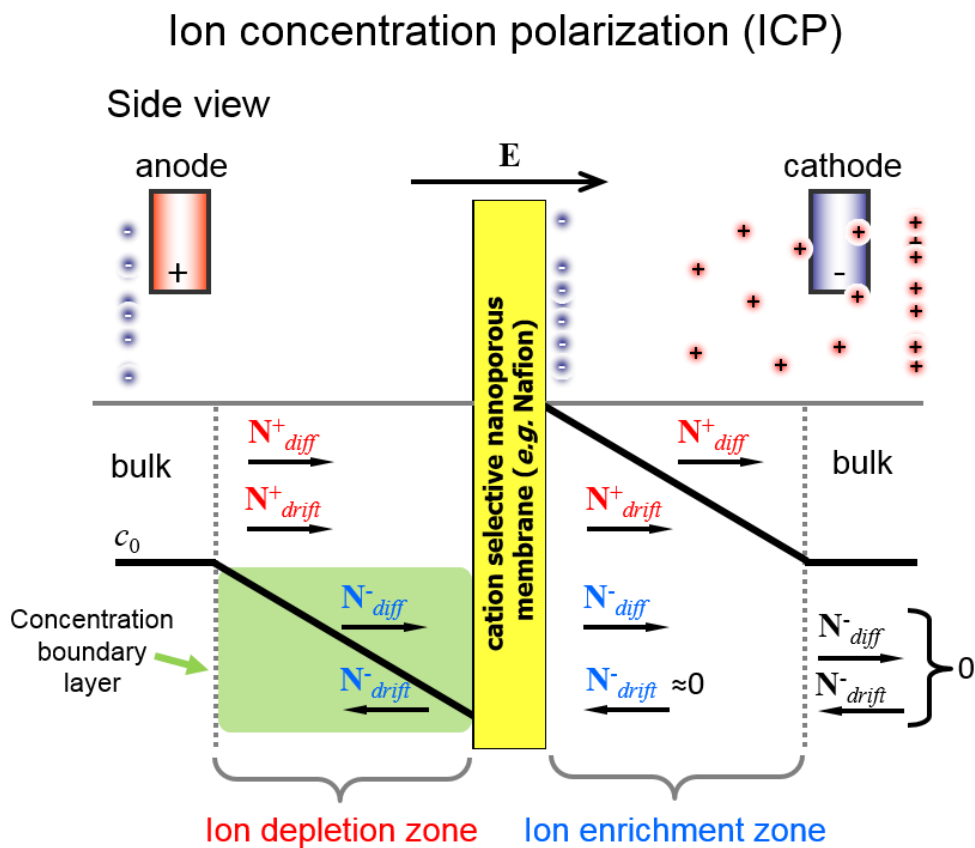


Figure 1.2. The schematic figure on principle of the ion concentration polarization (ICP) in the early model. N^+ and N^- are the number flux of cation and anion, respectively. ‘*diff*’ represents diffusion.

1.4 Diffusiophoresis

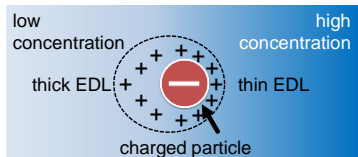
Diffusiophoresis is a natural migration of colloidal particle due to concentration gradient. The active investigations on the diffusiophoretic migration had led to various impressive applications. Especially, the colloidal particles were anomalously being excluded away from either nanoporous material[23], biological tissues[24], white blood cells[25] or hydrophilic monolayer[26], resulting in a particle-free zone of up to several hundred micrometers adjacent to the material/water interface even if there were no external driving forces.

Here, the concentration gradient was self-generated due to the permselective ion transportation toward the membrane with diffusivity difference of cations. When charged particles were immersed in an electrolytic solution with a concentration gradient, the particle propelled along the concentration gradient by two mechanisms: (i) chemiphoresis and (ii) induced electrophoresis[27-29]. Briefly, the concentration gradient induced an asymmetric EDL around the charged particles as shown in the first panel of Figure 1.3(a). Due to the asymmetric EDL, the electric field was self-generated (the second panel of Figure 1.3(a)) so that the particle migrated toward the high concentration region (the third panel of Figure 1.3(a)), which is called chemiphoresis. The second mechanism was based on the electric field induced by the diffusivity difference of dissolved ionic species rather than the asymmetric EDL. Typically, the diffusivity of different ions were unequal so that the diffusion rates of each ionic species were dissimilar. However, the electroneutrality should be held in the solution and, thus, an electric field was generated to retain the local electroneutrality as depicted in Figure 1.3(b). If particle was immersed in this environment, it transported along the induced electric

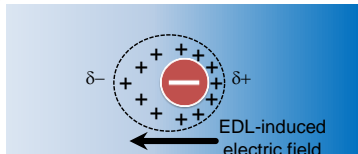
field. This phenomena is called as induced electrophoresis. The combination of the chemiphoresis and induced electrophoresis would provide the particle migration along the concentration gradient, called as diffusiophoresis.

(a) Chemiphoresis

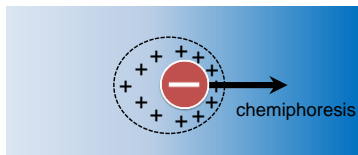
(i) Asymmetric electrical double layer (EDL)



(ii) EDL-induced electric field

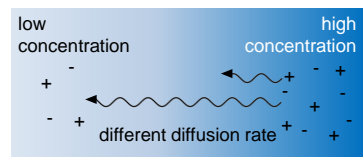


(iii) Particle migration



(b) Induced electrophoresis

(i) Diffusivity difference



(ii) Local electroneutrality unsatisfied



(iii) Electric field generated

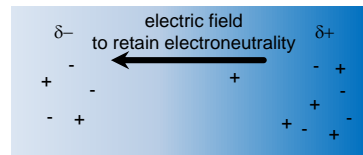


Figure 1.3. The schematic figure on principle of diffusiophoresis (chemiphoresis + induced electrophoresis)

1.5 Thesis objective

Concentration boundary layer is one of the key parameters when exploring micro-nanofluidic physics and engineering applications such as analyte preconcentration[30] or desalination system[31]. Concentration boundary layer can be defined as the layer where concentration gradient occurred due to permselectivity. This layer is important because the region owns different concentration from the bulk concentration leading to different electric field, flow field, electrophoresis, *etc.* However, concentration boundary layer had not been well established experimentally because of the difficulty of directly measurement of the concentration over the region. So, concentration boundary layer was usually deduced by observing other physical parameters such as particles movement, pH, IV curve[32, 33], *etc.* The major permselective ionic flux of ICP is electromigratory flux. Also, the major permselective ionic flux of diffusiophoresis is diffusive flux in equation (1.2). Both phenomena happened at the microchannel combined with nanoporous membrane junction. As mentioned earlier, this junction can affect the bulk concentration which arises concentration boundary layer.

In this thesis, concentration boundary layer caused by permselective ion transportation had been investigated. In chapter 2, 3 & 5 electromigratory flux was the main mechanism of concentration boundary layer, while in chapter 4 diffusive flux had been handled.

1.6 Thesis outline

In *Chapter 2*, a pseudo 1-D micro/nanofluidic device incorporating air valves at each microchannel was proposed for mitigating conventional limitations of 1-dimensional micro/nanofluidic device. Conventionally, a 1-dimensional micro/nanofluidic device, whose nanochannel bridged two microchannels, was widely chosen in the fundamental electrokinetic studies[34, 35]. However, the configuration had intrinsic limitations of filling and flushing the microchannel which was time-consuming and labor intensive tasks, due to the high fluidic resistance of the nanochannel bridge[36]. High Laplace pressure formed at liquid/air interface inside the microchannels played as a virtual valve when the electrokinetic operations were conducted. The identical electrokinetic behaviors of the propagation of ion concentration polarization layer and current-voltage responses were obtained in comparison with the conventional 1-D micro/nanofluidic device by both experiments and numerical simulations. The suggested pseudo 1-D micro/nanofluidic geometry was applied to chapter 3 to own not only experimental conveniences but also exact electrokinetic responses.

In *Chapter 3*, ICP was employed as the main background theory. Overall ICP process highly depends on the current transportation mechanisms such as electro-convection[18], surface conduction[37] and diffusio-osmosis[38] and the fundamental characteristics can be significantly altered by external parameters, once the permselectivity was fixed. In this chapter, a new ICP device with a bifurcated current path as for the enhancement of the surface conduction was fabricated using a polymeric nanoporous material. The material was protruded to the middle of a microchannel. While Nafion was exactly aligned at the interface

between two microchannels in a conventional ICP device[39]. Rigorous experiments revealed out that the propagation of ICP layer was initiated from the different locations of the protruded membrane according to the dominant current path which was determined by a bulk electrolyte concentration. Since the enhancement of surface conduction maintained the stability of ICP process, a strong electrokinetic flow associated with the amplified electric field inside ICP layer was significantly suppressed over the protruded membrane even at condensed limit. As a practical example of utilizing the protruded device, we successfully demonstrated a non-destructive micro/nanofluidic preconcentrator for fragile cellular species (*i.e.* red blood cells).

In *Chapter 4*, diffusiophoresis was employed as the main physical principle which was triggered by ion exchange process through the permselective interface. Concentration gradient near permselective interface was caused by diffusive flux with different cations' diffusivity. Since the repulsive force was induced by salt gradient only, the phenomenon can be applied to a microscale water purification platform without any external power sources[40]. In this chapter, we suggested a micro/nanofluidic device for continuous water purification utilizing the long-range diffusiophoretic migration around ion exchangeable surfaces. An ion concentration boundary layer was characterized by the Sherwood number (Sh) which is a key dimensionless number to describe the purification process. Depending on Sh , we experimentally demonstrated that the long-range diffusiophoretic exclusion can be applicable to the continuous water purification. Conclusively, our platform can commensurate with the high energy-efficient and portable water treatment operations such as purification, disinfection, water softening, *etc.*

Finally in *Chapter 5*, spatiotemporal concentration profile of diffusion-

convection layer during ICP process had been measured with patterned microelectrode. Here, diffusion-convection layer was defined as the intermediate region between bulk region and ion depletion zone. Unlike the traditional diffusion-convection layer which had linear concentration profile, the measured data indicated near plateau concentration distribution over the diffusion-convection layer in a microfluidic environment. The propagating plateau concentration profile with nearly 60 % of bulk concentration was confirmed with fluorescent dye visualization and microelectrode conductivity measurements, respectively. Also, three experimental parameters (fluorescent dye, bulk concentration and initial volumetric flow) were investigated to broaden the knowledge of plateau concentration.

Chapter 2. Pseudo 1-D Micro/Nanofluidic Device for Exact Electrokinetic Responses

2.1 Introduction

The original ICP device was usually consisted with the 1-dimensional serial connections of microchannel-nanochannel-microchannel[8, 34, 35]. However, the engineering applications of it required intensive modification of the original device for the desirable performances or functions. For example, the 2-dimensional connections for applying a tangential electric (or pressure) field[19, 41], the bifurcation of either or both microchannel for fractionating samples[31, 32] and the parallel connections of them for high-throughput multiplexing schemes[42, 43]. Even though it needed intensive modification, the original 1-D ICP device was still broadly chosen in fundamental electrokinetic researches, because the device had various advantages such as no uncontrollable pressure gradient across a whole domain and the convenience of tuning transport mechanisms, *etc.*

To be more specific, the original 1-D ICP device had intrinsic limitations such as the labor-intensive and time-consuming tasks of (1) filling samples and (2) flushing the device for initializing the electrolyte concentration. In usual, samples for the original device were filled before or after vacuuming process for the building block of silicon/glass or poly-dimethylsiloxane (PDMS), respectively[36]. A natural diffusion should be chosen as a mechanism for the flushing a sample through the microchannels, waiting more than several hours to re-use the device. One possible solution had been reported that thin side-microchannels were connected adjacent to the nanoporous membrane for the

convenience handling of the samples[37], but the I - V responses were inconsistent to that of the original device due to the residual flow through the side-microchannels. While the amplified electrokinetic flow pumped by the local high electric field[22] should be balanced with a backflow in the original 1-D ICP device[37], the amplified flows leaked through the side-microchannels in the device with the side-microchannels. Thus, the convective ion transportation was changed.

In this chapter, a new 1-D ICP device was proposed to resolve the limitations. We fabricated a pseudo 1-D ICP device by incorporating an air valve structure that utilized high Laplace pressure at the interface of liquid/air/(hydrophobic)solid as shown in Figure 2.1(a) and 2.1(b). The *in situ* propagations of ICP layer and its I - V responses were tracked in the original device, the pseudo 1-D device with and without the valve operation by both experimental and theoretical manners. Conclusively, all of electrokinetic responses in the original 1-D and the proposed pseudo 1-D ICP device (in the case of closing the air valve) were identical within experimental error bounds so that one would retain both experimental conveniences and exact electrokinetic responses with the pseudo 1-D device, promoting the researches for both fundamental nano-electrokinetics and its engineering applications.

2.2 The operation principle of the air valve

The 1-D ICP device incorporating with the side-microchannels near the nanojunction at the main microchannel had been utilized for easy-filling (or flushing) of samples[39]. However, uncontrollable leakage through the side-microchannels due to an amplified electrokinetic flow inside ICP layer hindered an exact measurement of electrokinetic fields. Here we added an air valve structure at both side-microchannels. As denoted in Figure 2.1(a), the device contained three electrolyte reservoirs and four air reservoirs. Main (red) and buffer (blue) microchannels were connected with a permselective nanojunction in Figure 2.1(b). Along the side-microchannels, there was a bifurcation of narrow and wide channels (the dotted square). The air valve based on a high Laplace pressure prevented the fluid leakages through the side-microchannels during ICP operations. The air valves were open/closed as following steps.

Step 1. Fill the samples from the main microchannel to the entire side-microchannels as shown in Figure 2.1(c). This was an “opening”-state of the air valve.

Step 2. By filling air from the air reservoir 1 (a narrow bifurcation), the samples along the narrow and wide microchannel would flow out toward the air reservoir 2 as shown in Figure 2.1(d). Due to the difference of the hydrodynamic resistance between the narrow and wide portion of microchannel, the fluid swept out as indicated as the magnitude of arrows. This was a “close”-state of the air valve. This step 2 was performed for both side-microchannels.

Note that the air filling (or applied pressure) was stopped once the meniscus was formed. The meniscus was theoretically able to endure the pressure more than 4000 Pa (approximately 40 cm of water column) with the given geometrical parameters based on the Young-Laplace equation, leading to a complete blocking of the leakage under a regular applied voltage.

When the liquid meniscus was formed in the side-microchannel, the withstanding pressure of the meniscus between the inside and the outside of the liquid can be calculated by the Young-Laplace equation as following:

$$\Delta P = P_{liquid} - P_{air} = -\sigma \left(\frac{\cos \theta_T + \cos \theta_B}{d_s} + \frac{\cos \theta_L + \cos \theta_R}{w_s} \right) \quad (2.1)$$

where P_{liquid} and P_{air} are the pressure at the interface of liquid and air, respectively and σ is the surface tension of water. θ indicates the advance contact angle of the water and the subscripts of T, B, L, R indicates the top, bottom, left, right surface of the side-microchannel, respectively. d_s and w_s are the depth and the width of the side-microchannel. Since water was chosen as the solvent and the microchannel was made of PDMS and glass substrate, we used values [44] of $\sigma = 74$ mN/m, $d_s = w_s = 15$ μm , $\theta_T = \theta_L = \theta_R = 118^\circ$, $\theta_B = 54^\circ$. When the meniscus was formed at the middle of the side-microchannel, the theoretical value of ΔP was calculated as 4048 Pa (40cm height of water column), which was large enough to withstand the pressure (P_{ind}) due to the amplified electrokinetic pumping. As shown in Figure 2.1(e) and 2.1(f), the meniscus was able to resist the electric body force with the applied voltage of 100 V which was much larger than the conventional driving voltage of ICP operation. In this work, θ_1 is almost the same as θ_2 and they should bigger than π – advance contact angle for stop the movement of meniscus. We

experimentally confirmed that they were bigger than 62° as shown in Figure 2.1(e) and 2.1(f). If the meniscus fail to stop at the middle of the side-microchannel, it advanced to the bifurcated point of the side-microchannel. In such case, the contact angle of the left and right side of the meniscus were reduced due to a diverging section. In other words, the meniscus was able to withstand higher pressure based on the new advanced contact angle [44]. The maximum pressure difference was obtained by substituting θ_L and θ_R with 180° in equation (2.1) resulting the new pressure difference as 9283 Pa (93cm height of water column).

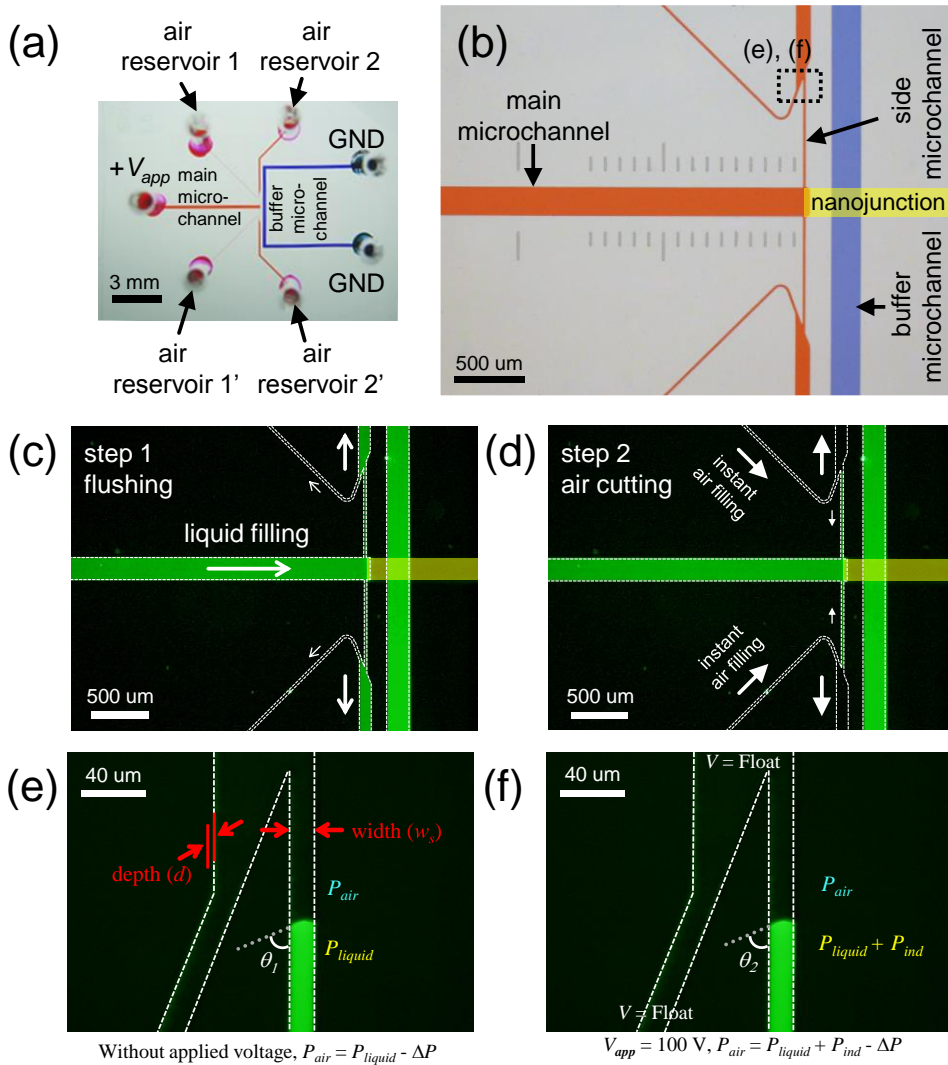


Figure 2.1. (a) Snapshot and (b) microscopic view of the fabricated pseudo 1-D ICP device. The sequences of operating air valve structures (c) Step 1: Flushing and (d) Step 2: Air cutting. The microscopic images of the meniscus at the air valve and its force balances (e) with and (f) without applied voltage. Here θ_1 and θ_2 were $\pi -$ (meniscus contact angle at the side PDMS wall without applied voltage) and $\pi -$ (meniscus contact angle at the side PDMS wall with 100 V applied voltage), respectively.

2.3 Experimental setups

General PDMS fabrication steps were used to fabricate microchannel structure (the main-and buffer-microchannel: 200 μm width X 15 μm depth, the side-microchannel of narrow region: 15 μm width X 15 μm depth and the side-microchannel of wide region: 100 μm width X 15 μm depth)[45]. The Nafion (Sigma Aldrich, USA) nanoporous membrane was patterned on the glass substrate based on surface patterning method[46]. On top of Nafion-patterned substrate, prepared PDMS molding block was irreversibly bonded to a designated position. A mixture of 1 mM KCl solution (Sigma Aldrich, USA) with sulforhodamine B (SRB) (25 nM, Sigma Aldrich, USA) as a fluorescent tracer and fluorescent micro-particles (diameter = 2 μm , Invitrogen, USA) were injected. The propagations of ICP layer were imaged by an inverted fluorescent microscope (IX53, Olympus) and CellSens program. Using Ag/AgCl electrodes, current-voltage responses were obtained by a source measure unit (Keithley 236, USA) and Labview program. The voltage sweep rate was 0.2 V/30 sec from 0 V to 10 V.

2.4. Results and discussion

2.4.1 The flow tracking with opening and closing the air valve

The generations of ICP layer were tracked *in situ* with opening and closing the air valve in order to confirm whether the fluid was leaked through the side-microchannels. As shown in Figure 2.2(a), the polystyrene beads as a flow indicator exited along the side-microchannels (indicated by yellow arrows) and the fluorescent intensity at the side-microchannel was diminished due to the leakage flow induced by ICP layer. Note that the leakage flow had a minimal amount of fluorescent dye, because most of dye would be filtered at the boundary of ICP layer. The air valve was opened and the applied voltage was 10 V in this demonstration. It had been reported that the electric field inside ICP layer was significantly amplified, leading ICP layer to strongly pump the fluid toward the nanojunction[22]. Since there were the side-microchannels near the nanojunction, the portion of the amplified flow would be leaked through the side-microchannels and the other turned back toward to the main-microchannel. In contrast, the particles were frozen inside the side-microchannels with closing the air valve as shown in Figure 2.2(b). Also the fluorescent intensity inside the side-microchannels was maintained, reflecting there was no leakage through the side-microchannel. These results strongly supported that there was no flow through the side-microchannel if the air valve closed. Consequently, the propagation of the depletion boundary (indicated by white arrows in each figure) was faster with closing the air valve than opening the valve.

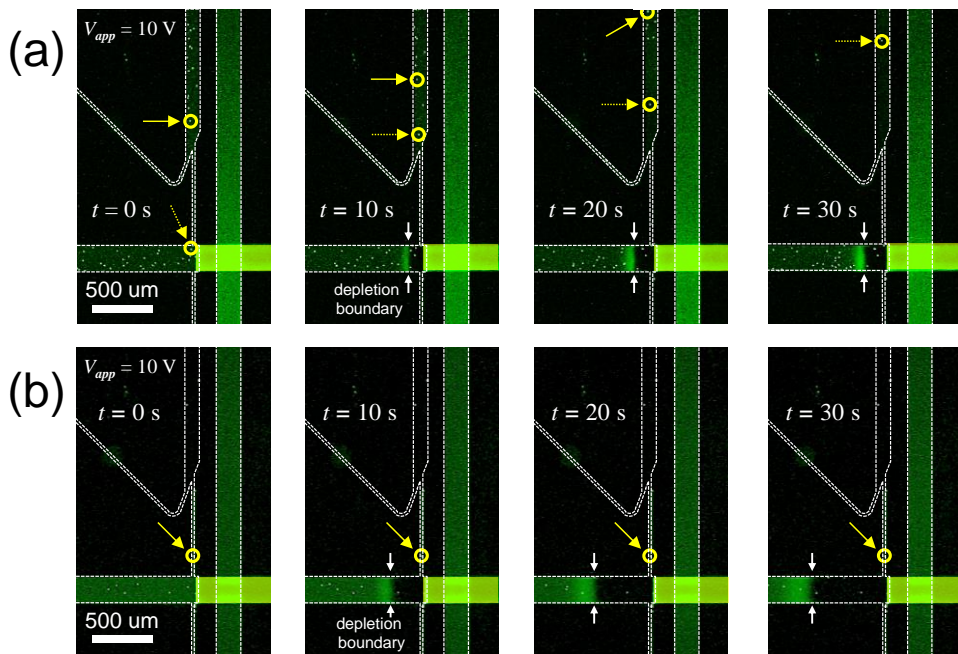


Figure 2.2. The movement of fluorescent microparticles and dyes at the applied voltage of 10 V with (a) the opening the air valve and (b) closing the air valve. In each figure, the depletion boundaries were denoted as two opposite white arrows.

2.4.2 The formations of the depletion boundary with opening and closing the air valve

The detailed formations of the depletion boundary for three distinct cases were shown in Figure 2.3. The external voltage was swept from 0 V to 10 V at the sweeping rate of 0.2 V per 30 s. Comparing three types of devices which were an original 1-D ICP device (the first column), a pseudo 1-D ICP device with closing the air valve (the second column) and a pseudo 1-D ICP device with opening the air valve (the last column), the original 1-D ICP device and the pseudo 1-D ICP device with closing the air valve had the identical propagation length of the depletion zone. On the other hand, opening the air valve would show much smaller propagation of the depletion zone than other cases. This was because the leakage was completely prevented by the air valve.

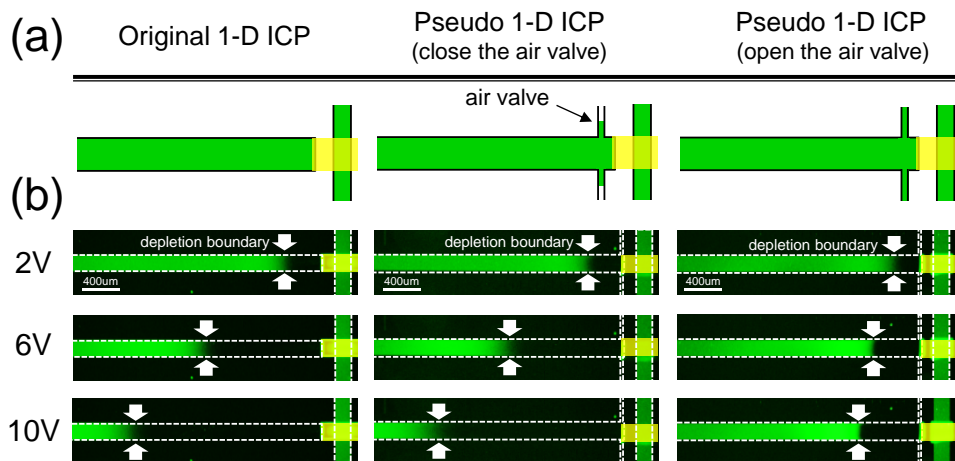


Figure 2.3. The propagation of the ion depletion zone in three different types of device. (a) Schematic diagrams of each device, (b) experimental results. The depletion boundaries were denoted as two opposite white arrows.

2.4.3 Current-voltage responses with opening and closing the air valve

The I - V responses were considered the most important characteristics of a system comprising a perm-selective nanoporous membrane. Under dc bias, a linear I - V relationship called Ohmic region was appeared and the plateau was followed due to the limitation of ionic carriers[47, 48]. This limiting current behavior was a nuisance in terms of an electrical power efficiency, since the current was saturated at the limiting value. Further application of voltage would lead to an overlimiting current behavior which was affected by various constraints such as a surface conduction[21, 37], an electroosmotic flow[17, 37, 49, 50] and an electroosmotic instability[6, 51]. These particular behaviors would imprint the signature of the system. Therefore, the I - V responses would be a fingerprint to identify the system. As shown in Figure 2.4, the I - V curve of the pseudo 1-D ICP device with closing the air valve (green) coincided with that of the original 1-D ICP device (blue). Since the measurements were repeated more than 20 times, the deviation of each plot were within the error bars. In contrast, the pseudo 1-D ICP device with opening the air valve had higher overlimiting conductance than others due to the suppressed depletion zone[39], while the Ohmic conductance were the same. This was because the most of leakage flow would initiate after the limiting current was reached and the suppressed ICP layer would result in the increase of conductivity inside the ion depletion zone[39].

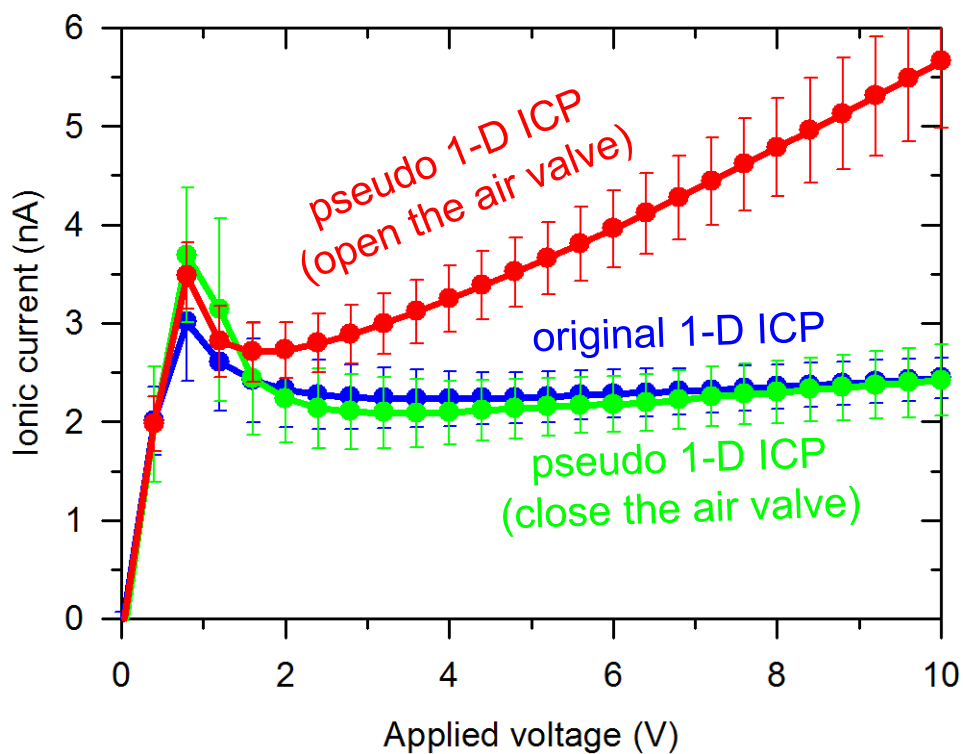


Figure 2.4. The current-voltage responses measured by experiments for three different types of device.

2.5. Conclusions

In this work, a new structural component for a fast and convenient experiment of a 1-D micro/nanofluidic device was proposed. The pseudo 1-D micro/nanofluidic device combined with the air valve not only reduced the total time of experiment but also provided the identical electrokinetic response with the original ICP device. The total time that took for one experiment include pre-process and run. The run times with the original and the pseudo device until the ICP reached steady state were identical (~40 minutes). However, the pre-process for resetting the electrolyte concentration inside microchannels took much shorter with the pseudo device than with the original device, because the reset only relied on a diffusion process with the original device. Thus, the time comparison for one experiment between the two devices was as follows.

Original 1-D device; pre-process (100 min) + run time (~40 min) = ~140 min.

Pseudo 1-D device; pre-process (1~2 min) + run time (~40 min) = ~45 min.

Therefore, if 10 data points are needed, it takes 1 day with original device and 7 hours 30 minutes with pseudo device.

We confirmed that there were no leakages at the interface of air-stop along the side-microchannel as long as the induced pressure \times surface area on the meniscus was smaller than the surface tension \times perimeter of the meniscus. In addition, the original 1-D ICP device and the pseudo 1-D ICP device with closing the air valve showed the identical formation of ICP layer and I - V responses, while the opening the air valve lead to the distorted results. Therefore, the presented method would provide an effective platform in the fundamental research of electrokinetic phenomena by eliminating the time-consuming and labor intensive tasks.

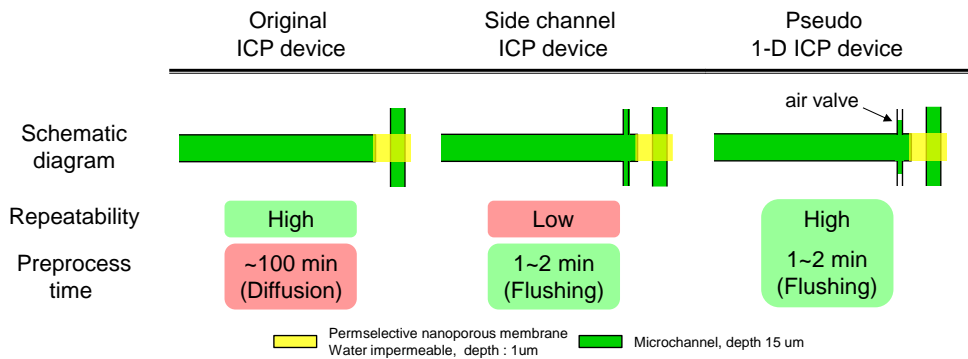


Figure 2.5. Comparison of repeatability and preprocess time of three different types of device. Proposed Air valve 1-D ICP device had high repeatability and short preprocess time.

Chapter 3. Ion Concentration Polarization by Bifurcated Current Path

3.1 Introduction

The fingerprinting evidence of ion concentration polarization (ICP) has been reported as the appearance of the Ohmic-limiting-overlimiting current regimes[17]. Especially, the source of overlimiting current, which was unable to be described by a conventional diffusion-drift theory[16], has been debated for a decade to include the dominance regime of extended space charge layer[48], surface conduction[21, 37], electro-diffusio-convection[17, 38, 49] and electroosmotic instability [52, 53]. Once the porous material has the permselectivity, the deterministic factors of distinguishing the regimes are external parameters such as the characteristic dimensions of bulk environment, the surface charges of building substrates and the bulk electrolyte concentrations[37]. If the externals become larger dimensions, lower surface charge and higher bulk concentration, the ICP phenomenon enter into the unstable regime[37]. Consequently, most of engineering ICP applications to concentrate bio-sample and to desalinate saline water would have been suffered from the unintended instability[54-56] since they utilized higher concentration than physiological fluids.

To avoid this nuisance, the underlying physics should be carefully investigated. The instability and the chaotic motions of the ion depletion zone are caused by the thermal fluctuation of the extended space charge layer and the amplified electric field inside the ion depletion zone with the absence of the surface conduction and the electro-diffusio-convection[52]. Thus, the instability would be mitigated by the enhancement of the surface conduction or electro-diffusio-convection. In this sense,

we artificially enhanced the surface conduction by coating a highly conductive polymer inside the microchannel. Since Nafion of the nanoporous membrane has high electrical conductance by itself, we let Nafion protrude along the microchannel so that there was an additional current path (or a bifurcated path) through the protruded part of Nafion, while Nafion was exactly aligned at the interface between two microchannels in the conventional ICP device. Lithographically fabricated nanochannels were unable to achieve this surface conduction enhancement because of a lower surface charge of substrates than one of Nafion (*e.g.* silicon, glass and PDMS $\sim 10\text{-}50\text{ mC/m}^2$ and Nafion $\sim 200\text{-}600\text{ mC/m}^2$). Rigorous characterization of this protruded device by experiments would be given in chapter 3 and, finally, a non-destructive preconcentration of fragile cells (red blood cell (RBC)) that required a stable ICP layer at high concentration and minimizing the shear stress due to strong electro-convection was successfully demonstrated.

3.2 Experimental setups

The design of the microchannel layout was similar to those devices that we have previously investigated as shown in Figure 3.1(a). On the main microchannel, we implemented the air valve structures which we had discussed in chapter 2. This allowed the main microchannel to become a dead-end microchannel so that one can conduct the experiment easily, while obtaining the exact electrokinetic response. The dimensions of the microchannel network were as follows: the main- and buffer-microchannel: $200\ \mu\text{m}$ width \times $15\ \mu\text{m}$ depth, the side-microchannel of narrow region: $15\ \mu\text{m}$ width \times $15\ \mu\text{m}$ depth, and the side-microchannel of wide region: $100\ \mu\text{m}$ width \times $15\ \mu\text{m}$ depth. The device were fabricated by conventional PDMS fabrication steps[45]. The Nafion (Sigma-Aldrich, USA) as a nanoporous membrane with high electrical conductivity, was patterned on the glass substrate using surface patterning method[37]. Briefly, Nafion was patterned by a simple straight microchannel ($200\ \mu\text{m}$ width \times $50\ \mu\text{m}$ depth) on a glass slide. Then, PDMS block having a microchannel network was irreversibly bonded by plasma bonder (CuteMP, Femto Science, Korea) to a designated position on top of the Nafion-patterned glass. Note that the protruded portion of Nafion membrane (denoted as L in the Figure 3.1(a)) should be aligned within the main microchannel under microscopic observations.

For visualization experiments, a mixture of KCl solution (Sigma-Aldrich, USA) at a concentration ranging from 0.1 mM to 1 M with Alexa Flour 488 (1 μM , Invitrogen, USA) as a fluorescent tracer were injected to both microchannels. pH of the KCl solution was measured to be around 5.6. Voltage was applied from the main microchannel reservoir via Ag/AgCl electrodes (a source measure unit,

Keithley 236, USA) to the buffer microchannel reservoirs, forming the ion depletion zone at the main microchannel. The propagations of ICP layer were imaged by an inverted fluorescent microscope (IX53, Olympus) and CellSens program.

Also two devices were fabricated for the measurement of the conductance between a nanoporous membrane and the electrolyte solution inside a straight microchannel. The first device was a simple straight microchannel with the geometries of 15 μm depth, 200 μm width, and 15 mm length (Figure 3.2(a)). The second one had a patterned nanoporous membrane at the bottom of the first device with ~ 1 μm height of Nafion nanoporous membrane (Figure 3.2(b)). The conductance of the second device would be the sum of microchannel and nanoporous membrane since the nanoporous membrane was paralleled with the microchannel.

The microchannel was filled and flushed with target concentration electrolytes for ~ 2.5 hours so that the impurities inside the microchannel to be eliminated and the nanoporous membrane to become equilibrium state. The voltage was stepped from -0.1 V to +0.1 V at the rate of 0.05 V / 60 s, where time current transients were saturated. The conductance of each devices with different electrolyte concentrations were determined by obtaining the fitting curve's slope (ionic current vs. applied voltage). Each measurements was repeated at least 5 times with 5 devices for reliability.

For current–time response measurements, a constant external voltage of 50 V were applied and the current values were automatically recorded at every 0.25 seconds by Labview program. 1 \times phosphate buffer saline (PBS) was chosen as a

test solution which is a buffer solution commonly used in biological research. Both visualization and I-t measurements were conducted at least 5 times with 5 different devices to ensure repeatability and reliability.

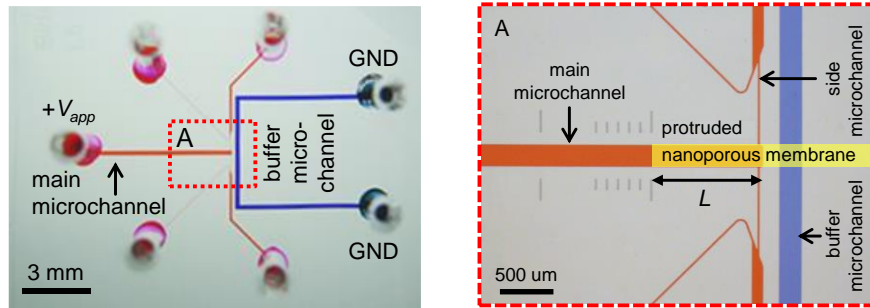
For non-destructive preconcentration experiments, human whole blood, 1 × PBS and 500 mM EDTA as the anticoagulant, was mixed at a volume ratio of 1:50:0.5 as a target sample.

3.3 Results and discussion

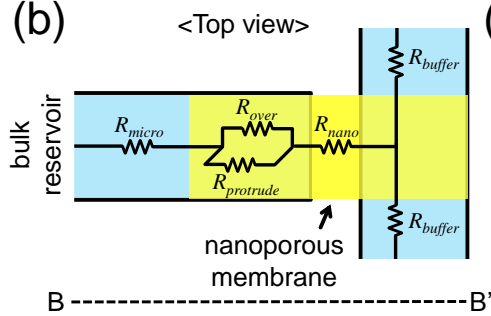
3.3.1 The characterization of bifurcated current path with equivalent circuit

Microscopic snapshot of the micro/nanofluidic device having the protruded nanoporous membrane was shown in Figure 3.1(a). The length of the protruded nanoporous membrane was denoted by L . While conventional nanoporous membrane was positioned right at the end of the microchannel substrate, *i.e.* $L = 0$ μm , the nanoporous membrane was intentionally protruded from the end of the microchannel substrate in this device. For example, the devices of $L = 0$ μm , 1000 μm , 3000 μm or 6500 μm were fabricated depending on the experimental needs. By installing the protruded membrane, one can expect that the path of ionic flux was bifurcated as described by the equivalent circuit model. Schematics of top and side view of the proposed devices with equivalent electrical resistors were shown in Figure 3.1(b) and 3.1(c), respectively. R_{micro} and R_{buffer} represented the resistors of the main and buffer microchannel. R_{nano} referred the resistor of the nanoporous membrane between the main and buffer microchannel. While R_{over} and R_{protrude} had been ignored in a conventional nanofluidic device, they appeared in this device since the highly conducting membrane was protruded, leading to the bifurcated current path. Since ionic current tended to pass through the lower resistor, the ratio of R_{over} to R_{protrude} played the significant role to determine the effective current path and the location where ICP was initiated. Here, R_{protrude} was fixed by the material property of the membrane and R_{over} was inversely proportional to the electrolyte concentration inside the microchannel so that the current path highly depended on the electrolyte concentration.

(a)



(b)



(c)

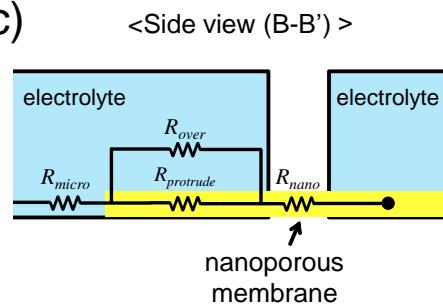


Figure 3.1. (a) Snapshot and microscopic view ((A) in red box) of the fabricated non-destructive cellular preconcentrator. L was the length of protruded nanoporous membrane from the main microchannel. Schematics of (b) top and (c) side view of the proposed devices with equivalent electrical resistors (not to scale).

3.3.2 The conductance measurement between a nanoporous membrane and the electrolyte solution inside a microchannel

In order to characterize the dependency, two microfluidic devices were fabricated for the comparison of the conductance between a nanoporous membrane and the electrolyte inside a microchannel. The first device was a simple straight microchannel (Figure 3.2(a)) and the second device was composed of a patterned nanoporous membrane at the bottom of the simple straight microchannel (Figure 3.2(b)). Detailed dimensions of the devices and the measurement method were described in chapter 3.3. The appearance of plateau is attributed to electric double layer (EDL) overlap phenomenon which becomes severe as the bulk concentration decreases. Since fixed amount of counter-ions existed inside the nanoporous membrane with the severe EDL overlap, the ionic conductance of the nanoporous membrane was independent from the bulk concentration [7, 8].

This estimation was applied to the protrude membrane device to identify the effective path of ionic flux passing through either the protrude nanoporous membrane or the microchannel. The calculated ionic conductance were plotted in Figure 3.1(d) as a function of the electrolyte concentration ranging from 1×10^{-4} to 1 M. As a result, the dominant path of ionic flux was bifurcated near 50 mM in the device. In other words, the current dominantly conducted through the protrude membrane at the concentration lower than 50 mM and *vice versa*.

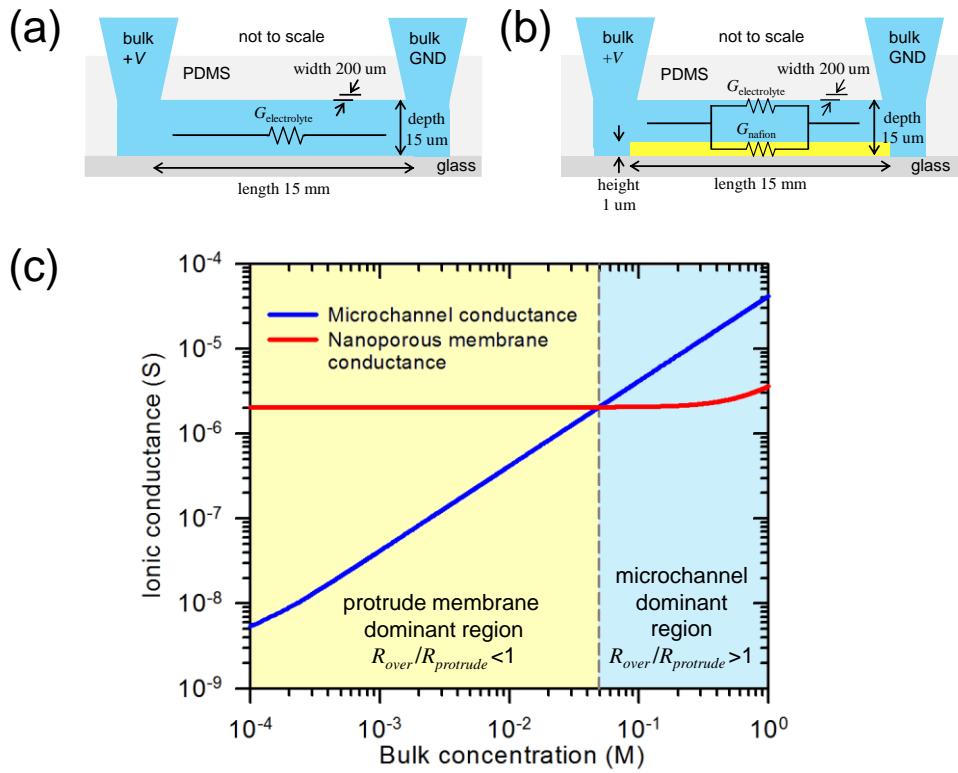


Figure 3.2. Side schematic view of (a) simple straight microchannel device and (b) the device with patterned nanoporous membrane at the bottom. (c) Calculated ionic conductance of microchannel and nanoporous membrane.

3.3.3 The propagation of ICP layer upon bifurcated current path

The bifurcated path was confirmed by the visualization of ICP layer formation. The experiments were conducted with the protruded nanoporous membrane of $L = 1000$ μm . Three different electrolyte concentrations were selected as representative values based on the data in Figure 3.1(d); (i) dilute limit: 1 mM for nanoporous membrane dominant regime ($R_{\text{over}}/R_{\text{protrude}} > 1$), (ii) condensed limit: 1000 mM for microchannel dominant regime ($R_{\text{over}}/R_{\text{protrude}} < 1$), and (iii) 31.6 mM for intermediate regime ($R_{\text{over}}/R_{\text{protrude}} \approx 1$). The time-revolving snapshots of propagating ion depletion zone (or ICP layer) at each concentrations were shown in Figure 3.3(a)-3.3(c). The schematic connections using the equivalent circuit were also given below each figures. Red line indicated the dominant current paths.

At dilute limit (1 mM), the propagation of the ion depletion zone started at the end of the protruded nanoporous membrane (Figure 3.3(a)) and expanded toward both directions. The propagation toward anodic side (red arrow) was similar to the conventional propagation, where the amplified electric field and chaotic electro-convection mixed the electrolytes[22]. However, a reverse propagation toward the cathodic side (yellow arrow) was also observed. This propagation was comparatively slow and the boundary moved nearly zero velocity. The main factor for the slow propagation was due to near zero electric field above the protrude membrane. Because the conductance of nanoporous membrane was much higher than that of microchannel in the dilute limit, the preferential path of the ionic current should be through the protruded membrane, *i.e.* no strong electro-convection over the membrane. As a result, the diffusion was the only driving force for the propagation (yellow arrow), leading to the blurred boundary, while the propagation due to a strong electro-convection (red arrow) had a sharp boundary.

On the contrary, the propagation started from the end of the microchannel (white arrow) and expanded until the zone met the end of protruded membrane in the case of condensed limit (1 M) (Figure 3.3(b)). Typically, the propagation characteristics of the ion depletion zone in highly concentrated limit such as over 100 mM can be explained as unstable, slow propagation, and short ion depletion zone length[54, 56]. Noteworthy, stable and lengthy propagation of the ion depletion zone was observed over this protruded membrane, because the current path was formed through the membrane. However, once the depletion zone escaped the membrane ($t > 20$ sec in Figure 3.3(b)), strong electro-convection reappeared, since the concentration above the protruded membrane became diluted and behaved as the conventional propagation with strong vortex.

At an intermediate concentration (31.6 mM), the propagation started at both ends of protruded membrane and the microchannel. (Figure 3.3(c)), showing like a merged picture of the dilute limit and the condensed limit. These phenomena can also be explained by the resistance ratio between microchannel and nanoporous membrane (R_{over} and $R_{protrude}$ in Figure 3.1(c)). In the case of $R_{over}/R_{protrude} \approx 1$, the current path would be formed every points along the membrane, but the electric field at the ends of protruded membrane and the microchannel would be amplified due to geometric focusing (or edge) effects so that two current paths were competing to induce two ion depletion zones.

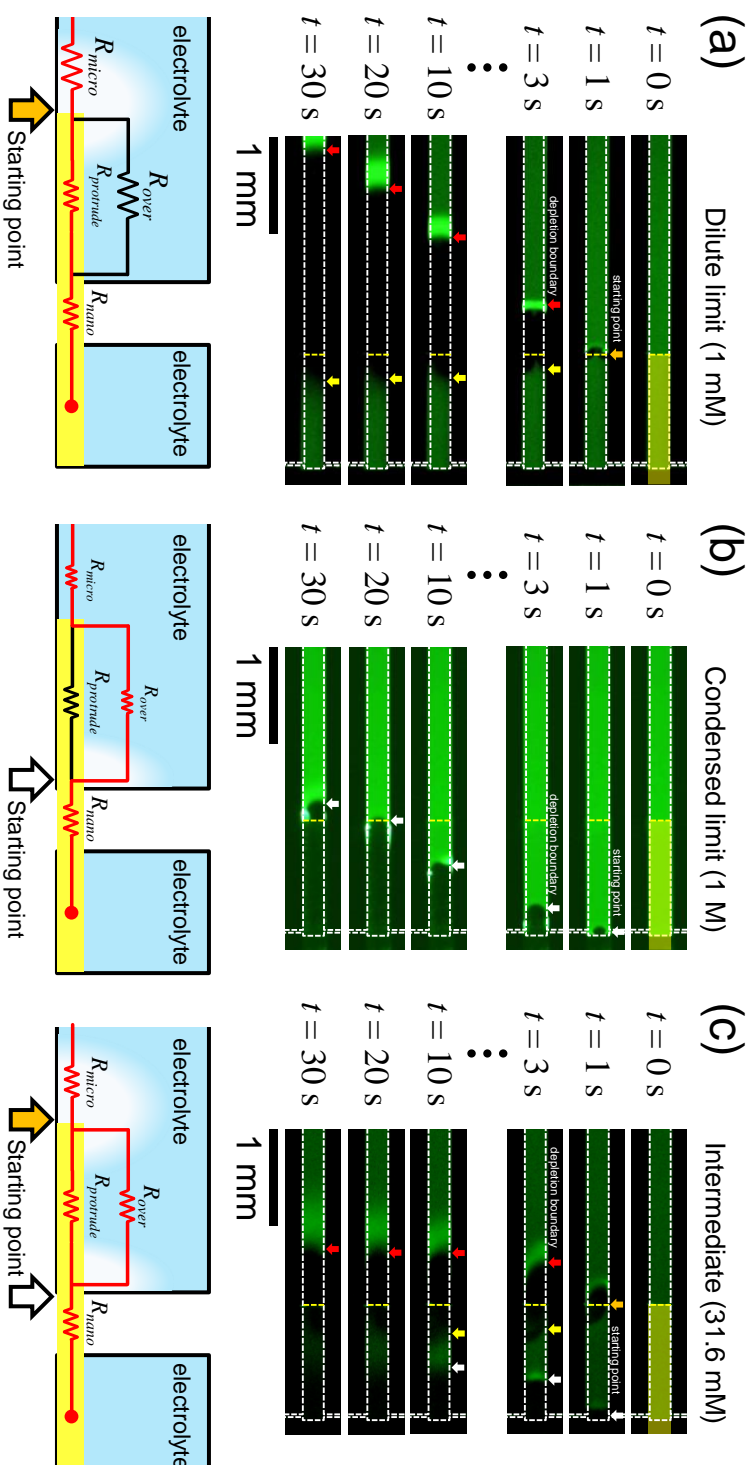


Figure 3.3. Time-revolving snapshots of propagating ion depletion zone (or ICP layer) at each concentrations with the applied voltage of 50 V; (a) Dilute limit (1 mM), (b) condensed limit (1 M) and (c) intermediate (31.6 mM). The schematic connections with the equivalent circuit were also given below each figures (not to scale). Red line indicated the dominant current paths.

3.3.4 I-t responses upon bifurcated current path

To explore the mechanisms of how the current level changes as the ion depletion zone propagates, I-t responses were measured at $0.01 \times$ PBS media (~ 1.5 mM; dilute limit) and $1 \times$ PBS media (~ 150 mM; condensed limit) with the various protruded length. We selected PBS since it was common biological buffer solution and the concentration of $1 \times$ PBS (~ 150 mM) was laid in the condensed limit.

In the case of dilute limit, the depletion zone started from the end of protruded membrane so that the current dropped immediately and decayed exponentially for all protruded length as shown in Figure 3.4(a). The device in the inset had $L = 3000$ μm . This was because the remaining portion of solution over the membrane merely affected on the current path. Thus, all of data converged into the case of non-protrude membrane ($L = 0$ μm).

On the contrary, at the condensed limit, the ion depletion zone started at the end of the microchannel quickly propagating toward the anodic side (A~C in the inset of Figure 3.4 (b)) and the propagation was slowed down once the boundary reached the end of membrane (D~E in the inset of Figure 3.4 (b)). The device in the inset had $L = 3000$ μm . This observation taught us that the propagation was divided into two stages. This was also confirmed by the I-t drops as well in Figure 3.4 (b). See the line of $L = 3000$ μm as a representative example. The first current drop had low rate while the ion deletion zone boundary moved over the protruded membrane (A~B in Figure 3.4 (b)). The second stage had the high rate of current drop, where the boundary was located outside the protruded membrane (D~E in Figure 3.4 (b)). In the first stage, even though the ion depletion zone length increased dramatically (0 μm to 3000 μm), the current only decreased to one third of its initial value. In the

second stage, there was a small increment of the ion depletion zone length (3000 μm to 3350 μm) but the current decreased dramatically to one fiftieth of its initial value. Conventionally current decreased rapidly with the formation of the ion depletion zone like the behavior in the second stage or the behavior of $L = 0$ μm case. This was because of the rapid concentration drop inside the depletion zone, resulting extremely high electrical resistance and the amplified electric field inside the depletion zone[22]. In the second stage, the current was passing mostly through the protruded membrane even in this condensed limit because the electrolyte concentration over the membrane was significantly depleted. In summary, since the conductance of the protruded membrane was fixed in the first and second stage, the main current path would be changed from the electrolyte solution over the membrane in the first stage to the membrane in the second stage. In the first stage where the current decreased slowly, the effective conductance of the ion depletion zone maintained higher than that of conventional depletion zone with the aid of the constant conductance of the protruded membrane. That is to say, once the depletion zone was initiated (*i.e.* R_{over} started to increase), the most of current started to conduct through $R_{protrude}$, since R_{over} and $R_{protrude}$ were connected in parallel. Therefore, the magnitude of local electric field over the protrude membrane in the first stage was significantly less than that in the conventional device, leading to the minimal magnitude of amplified electrokinetic flow inside the zone and its associated shear stress near the zone.

In the following chapter, a non-destructive cellular preconcentrator was demonstrated with extremely long protrude membrane for maximizing the first stage.

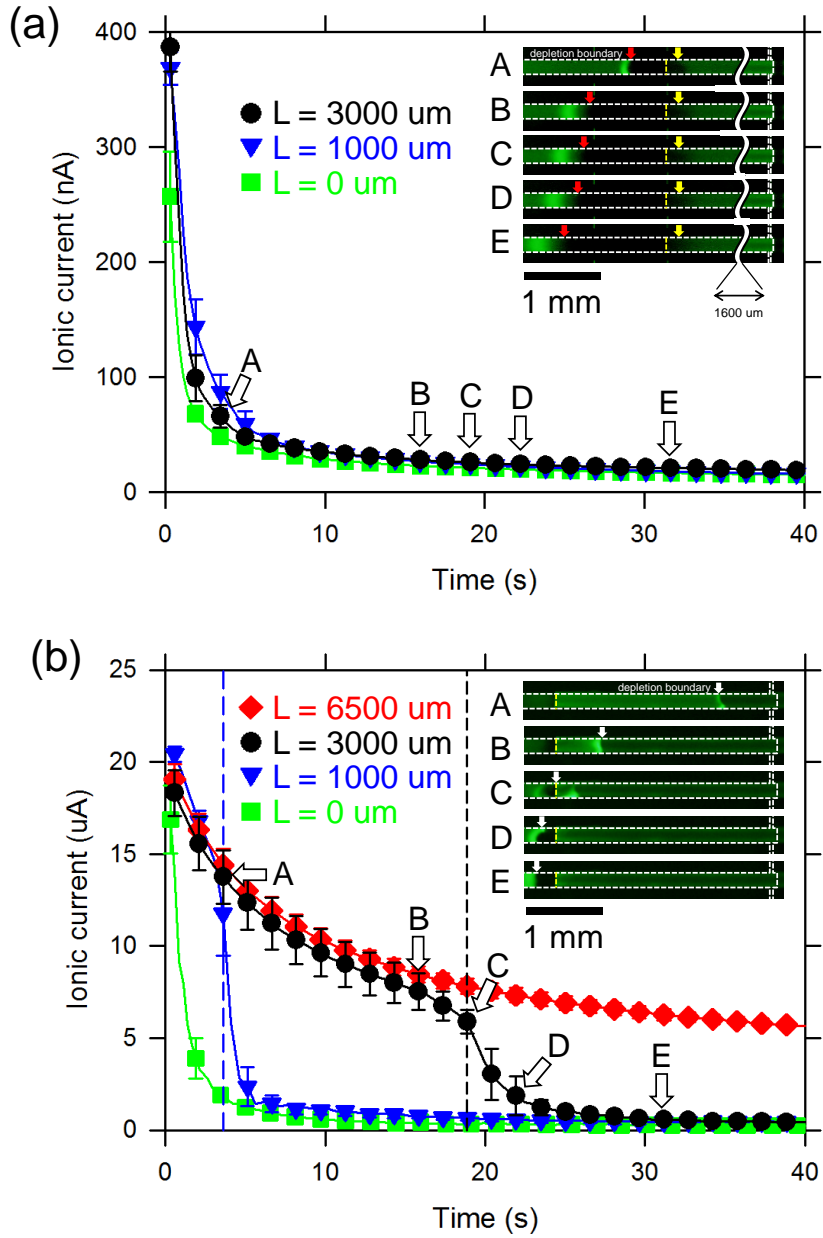


Figure 3.4. Current-time responses of (a) $0.01 \times$ PBS media (~ 1.5 mM; dilute limit) and (b) $1 \times$ PBS media (~ 150 mM; condensed limit) with the various protruded length. Each figures had an inset of microscopic views in the case of $L = 3000$ μm . Capital letters indicated the time at which the snapshot were taken.

3.3.5 Non-destructive cellular preconcentrator

ICP had been utilized as an efficient biomolecular preconcentration mechanism[57]. Unlike a preconcentration mechanism using a free-flow concept such as isotachopheresis[13] and field amplified stacking[58], the amplification ratio of ICP preconcentrator would be up to million-fold since the target molecules was supplied from a reservoir of nearly infinite volume compared with the volume of microchannel[19]. While various (bio-)molecules such as fluorescent dyes[41, 59], DNAs and aptamers[43], *etc.* were successfully preconcentrated with noticeable factor, there are intrinsic limitations to be solved. First, most of the device using ICP phenomenon has been operated at low bulk concentration which can cause the modification or destruction of the biosamples due to osmotic pressure in the case of cellular species[60]. The main reason of using a low bulk concentration was due to the instability and the chaotic motion of the ion depletion zone in high bulk concentration which hindered the stable formation of ICP layer [31, 54]. Secondly, significantly amplified electric field[22] inside the ion depletion zone caused strong vortical flow to induce a high shear stress at the boundary of the ion depletion zone[17, 49], destructing the target samples during ICP preconcentration process. Since most of cells were wrapped with a lipid bilayer membrane, which is only a few nanometer in thickness[61], such cells with fragile membrane were destructed during the ICP preconcentration. Note that the shear stress of the vortex in a conventional ICP operation would increase up to 10 Pa (shear stress = water viscosity \times velocity gradient = 0.001 Pa \cdot sec \times O(10) mm/sec / O(1) μ m)[17]. Thus, additional treatment was required for the prevention of the destruction[60] but this process removed the original properties of the species blurring the final analysis results. Since the protrude membrane minimized the

amplified electric field inside ICP layer which is directly proportional to the velocity gradient, the presenting device would be an appropriate platform for those weak cellular species.

Recently, there has been an increasing demand for a device that allows rapid blood testing anywhere, along with the growing need for point of care testing or the aim for expansion of blood testing in developing countries where the medical equipment is inadequate. Essential component of such device would be a plasma separator without loss of RBC. Since a centrifugal separation causes serious hemolysis of RBC, an efficient recovery of RBC with non-centrifugal separation would cut the volume of blood drawn to half. In this section, we would demonstrate the preconcentration of RBC without any damage.

The preconcentration of RBC out of diluted human whole blood with $1 \times$ PBS was provided for the demonstration of the non-destructive preconcentration process. Devices with protruded membrane ($L = 1000$ μm in Figure 3.5(a) and $L = 6500$ μm in Figure 3.5(b)) were utilized in this section. The sequential snapshots of RBC preconcentration were presented for each devices. Unlike other sections which adopted closed air valve at both side-microchannels, the air valve was opened for continuous supply of sample RBCs.

Alike the condensed limit in Figure 3.3(b), RBC migrated toward anodic side as the ion depletion propagated ($t = 0 \sim 8$ sec) in both Figure 3.5(a) and 3.5 (b). Since the ion depletion zone acted as a virtual barrier to the charged species, RBCs should be rejected to enter the zone so that it should be accumulated at the boundary of the ion depletion zone. In the meantime, there was minimal amplified electric field over the protruded membrane due to the bifurcated current path. Herein there were no destruction of the blood cells in both cases. However, as the depletion

zone escaped from the protruded membrane, the current path through the solution over the protruded membrane was eliminated and the strong vortical flow was formed at the end of the membrane, causing the destruction of RBCs in Figure 3.5(a) from $t = 12$ sec. While it had been reported that the threshold shear stress of hemolysis was ~ 100 Pa at few milliseconds exposure time [62-64], hemolysis was occurred with the vortex by ICP (shear stress = ~ 10 Pa) due to the combined effect of osmotic expansion of RBCs and longer exposure time. Low concentration inside ICP layer induced an osmotic pressure from outside to inside the RBCs so that they were expanded and the expansion was observed (The shadows of bi-concave shape would be diminished when the RBC met the boundary of ICP layer). Note that the red region at the end of the membrane included the pre-concentrated hemoglobin which was leaked from the RBCs as hemolysis occurred (Figure 3.5(a), $t = 50$ sec).

Unlike the device of $L = 1000$ μm , there were no destruction at all in the device of $L = 6500$ μm (Figure 3.5 (b), $t = 12$ sec and 50 sec). Because there existed the bifurcated current path all over the microchannel, stable and non-destructive pre-concentration of the RBCs was achieved. The amplification ratio of RBCs were ~ 40 fold. Note that the steady state length of the ion depletion zone with the applied voltage of 50 V was in the range from 1000 μm to 6500 μm .

In terms of the current path, the schematic diagrams of developed ion depletion zone at $t = 50$ sec for each cases were depicted in Figure 3.5(c) and Figure 3.5(d), respectively. In the diagrams, equivalent electrical resistance with different size representing different resistance were also described. The color of major current path was indicated in red. As the ion depletion zone escaped from the protruded membrane, the resistance of the ion depletion zone outside the nanoporous membrane (R_{depl}) became the largest resistance along the current path. Also the

R_{dep1} was the main factor of the destruction of cellular species during preconcentration process. It induced the amplified electric field and chaotic motions, leading to high shear stress on the species. On the other hand, there was no such R_{dep1} in Figure 3.5(d). In other words, there was minimal amplified electric field and chaotic motions due to the bifurcated current path. As a result, minimal shear stress was applied on the species enabling a stable preconcentration without destruction.

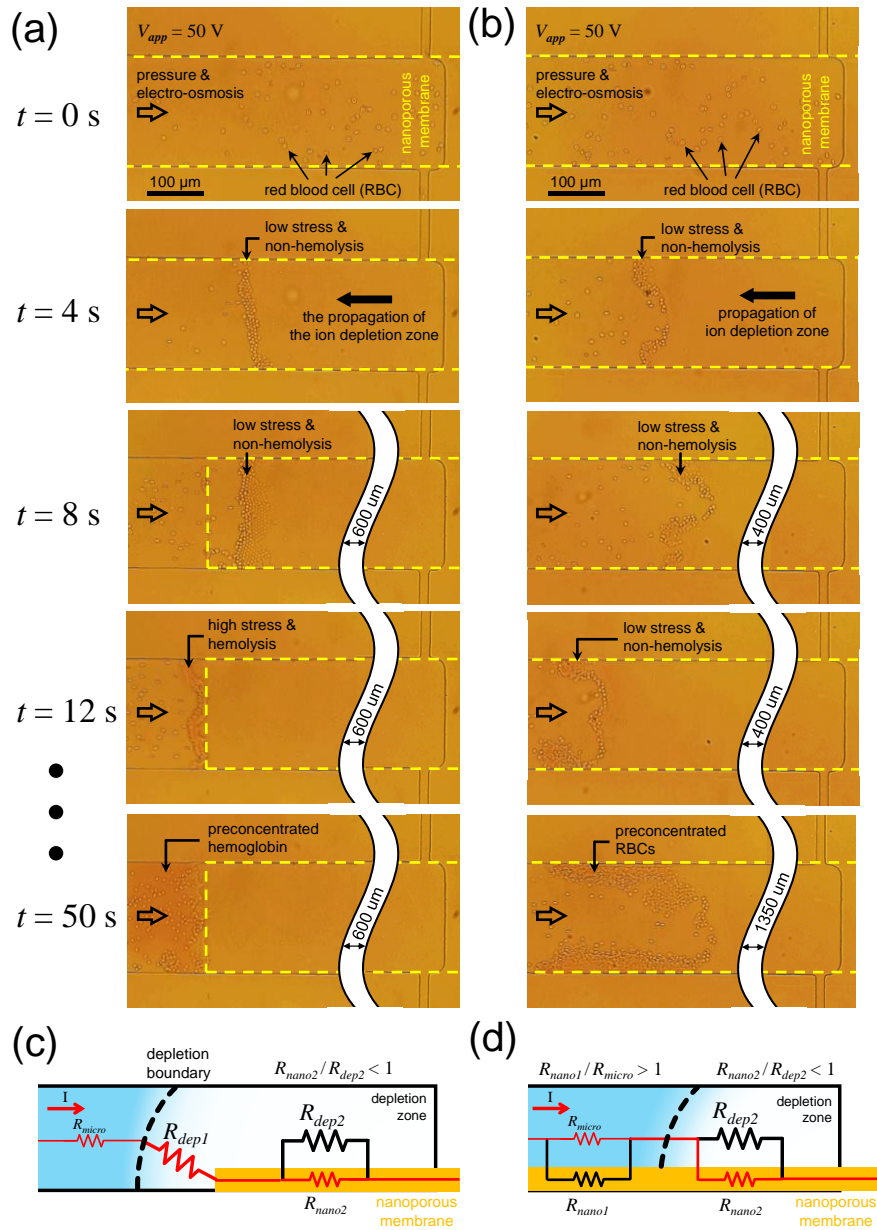


Figure 3.5. Time-evolving snapshots of RBC preconcentration with the devices of protruded membrane length (a) $L = 1000 \mu\text{m}$ and (b) $L = 6500 \mu\text{m}$. The amplification ratio of RBCs were ~ 40 fold in (b), while most of RBCs were destroyed in (a). In terms of the current path, the schematic diagrams of developed ion depletion zone at $t = 50 \text{ sec}$ for each cases were depicted in (c) and (d) (not to scale).

3.4. Conclusions

The research of ICP has focused on unveiling the fundamental electrokinetic processes near a perm-selective membrane. Also, various engineering endeavors recently conveyed several innovative applications using these processes. In this work, the protruded membrane was fabricated in the micro/nanofluidic ICP platform to greatly enhance the surface conduction of the ionic current which is the essential key of suppressing the unwanted instability and high shear stress due to the amplified electrokinetic responses. Experimental visualizations revealed that the ICP layer was initiated from either the end of protruded membrane or the end of microchannel at the dilute limit or the condensed limit, respectively. Current-time measurements and numerical simulations were carried out to verify that the effect of conductance ratio of the electrolyte to the membrane. Consequently, the strong electrokinetic flow associated with the amplified electric field inside ICP layer were significantly suppressed over the protruded membrane at the condensed limit. Using the protruded device, we successfully demonstrated a non-destructive micro/nanofluidic preconcentrator of RBCs. Conclusively, promoting the surface conduction by coating of additional conductive material would successfully suppress the unwanted instability so that the presenting protruded device would be utilized as an effective mean for stabilizing the ICP process even at 1 M concentration and regulating the inherently amplified electrokinetic flow inside ICP layer.

Chapter 4. Diffusiophoretic Exclusion of Colloidal Particles for Continuous Water Purification

4.1 Introduction

Recently, diverse natural (or self-driven) phenomena have been extensively applied for various interesting physicochemical research fields[65-70]. Among the striking phenomena and these applications, the natural migration of colloidal particle under imposed or self-generated concentration gradient, which is called as diffusiophoresis, has been drawn significant attentions up to date. Classically, total ion concentration (*i.e.* proton, non-protonic cation and anion) outside the ion exchange medium had considered as constant because one proton was exchanged with one non-protonic cation. However, due to the difference of their diffusivity, the diffusive flux of H^+ is typically larger than the flux of non-protonic cation. Although the 1:1 ion exchange occurs through the exchange surface, the total ion concentration adjacent to the nanoporous medium spontaneously decreases[71, 72] since the both fluxes are generated in the opposite directions. The concentration gradient drives the effective migration of colloidal suspension based on diffusiophoretic manner (chemiphoresis + induced electrophoresis). The detailed mechanism of diffusiophoresis can be found in other literatures[27-29, 73, 74] The active investigations on the diffusiophoretic migration have led to various impressive applications such as microfluidic microdialysis[75], soluto-inertial beacon[76], diffusiophoretic particle focusing[77, 78], membraneless water filtration[40], low cost zeta potentiometry[79] and diffusiophoretic self-swimmer[80], *etc.* Although many investigations and hypotheses about the peculiar

long-range exclusion have been studied for decades[23, 26, 81-85], the exact physical origin has remained unclear until recently. However, Florea and coworkers[71, 86]unraveled the driving force which was related to the diffusiophoretic migration induced by an ion exchange process through the material/water interface.

To resurrect this fundamental physics into a practical micro/nanofluidic platform, we suggested a continuous water purification system (*i.e.* elimination of immersed colloidal particles from source water). In this chapter diffusiophoretic exclusion around the ion exchangeable interface was pivotally utilized without any external stimuli. Basically, our physical principles were similar to that of Shin's work[40] but the gradient-generating method was totally different (CO₂ dissolution in Shin's work vs. ion exchange in this work). Utilizing ion exchange would be helpful to simplify the device and to miniaturize micro/nanofluidic water purification platform since there is no need of controlling gas pressure balance between air and CO₂ channel. The micro/nanofluidic device was fabricated to initiate the ion exchange and the long-range diffusiophoretic exclusion. As colloidal particles immersed in electrolyte solution were introduced into the device, the particles were repelled from the Nafion walls (cation-exchange medium) by the diffusiophoretic mechanism due to an ion concentration boundary layer triggered by the ion exchange process. A rigorous boundary layer model with the Sherwood number, which is dimensionless number correlating most of physicochemical parameters (flow rate, diffusivity of ionic species and geometrical factors), was developed to quantitatively elucidate the purification process, although similar exclusion experiment was qualitatively demonstrated[87]. Thus, our analysis and experimental verifications enabled one to explain the intriguing microscale water

purification process more clearly. Conclusively, diffusiophoretic exclusion of colloidal particles would be an effective mean for energy-efficient and portable water purification as well as conventional use of ion exchange process such as desalination or water softening.

4.2 Experimental setups

Two pieces of Nafion sheets ($1.5 \text{ mm} \times 30 \text{ mm} \times 0.175 \text{ mm}$, Sigma-Aldrich, USA) were aligned on the slide glass with finite interval. The alignment was performed under the microscopic observation and the interval varied for each devices from $300 \text{ }\mu\text{m}$ to $800 \text{ }\mu\text{m}$. Four layers of commercial 3M tapes (the layers had $200 \text{ }\mu\text{m}$ thickness) were positioned at the end of the Nafion sheets as shown in first step of Figure 5. Next, one layers of 3M tape were attached to fix the aligned Nafion sheets as shown in second step of Figure 5. On top of the Nafion and 3M tape substrates, prepared blank PDMS block with punched holes were irreversibly bonded using oxygen plasma treatment (CuteMP, FemtoScience, Korea) as shown in third step of Figure 5. As reported by Kim and coworkers[88], there must be an incomplete bonding at the edges of the Nafion sheets. In order to eliminate the incomplete bonding, uncured PDMS was squeezed to fill the edges. Then the device was placed on the hot plate for the stabilization of plasma bonding and solidification of uncured PDMS. Lastly, inlet and outlet were connected to the device as shown in fourth step of Figure 5. Note that the fabrication method was simple and even the soft lithography was unnecessary during the fabrication steps.

For the experimental demonstrations, 1 mM or 100 mM NaCl solution (Sigma-Aldrich, USA) was injected through the inlet. The device went through a desiccation process in a vacuum chamber for 20 minutes to prevent the formation of air bubbles inside the microchannel during the sample filling. External flow rate was determined by a syringe pump (PHD2000, Harvard Apparatus, USA). Alternatively, liquid level difference between inlet and outlet reservoir could also be utilized for power-free purification concept. Depending on the distance between

two Nafion sheets, the introduced flow rate was varied to control the Sherwood number of the system. The distance between the sheets was calculated by averaging at least seven different points. Also, swelling and shrinking of the Nafion sheet with evaporation of the collected sample were considered as well. The collected sample was diluted with deionized water to satisfy the minimum volume requirement of the ion chromatography (DIONEX ICS-1100, ThermoFisher, USA) and the cation concentration was recalculated using at least five reference electrolytes near the data. pH of collected sample was obtained using universal pH indicator (Science Lab, Universal Indicator Solution, catalog #SLU1051). The fluorescent particles (fluorescent polystyrene microspheres, diameter = 1 μm , ThermoFisher, USA) were used for particle exclusion experiments and their motions were imaged by an inverted fluorescent microscope (IX53, Olympus, Japan) and CellSens program (Olympus, Japan).

4.3 Results and discussion

4.3.1 Concept of micro/nanofluidic water purification

It has been known that if a colloidal suspension is introduced into a microchannel of which side walls were composed of ion exchange medium (*e.g.* Nafion, nanoporous hydrogel or highly charged nanoporous materials), an ion exchange process between ionic species with different diffusion-rate triggers decrease of ion concentration[71] as depicted in Figure 4.1(a). An arc-shaped ion concentration boundary layer is developed along y -direction due to ion exchange and ion diffusion together with convectional flow as shown in Figure 4.1(b). Because of the concentration gradient inside the layer, the immersed colloidal particles would migrate away from the nanoporous medium depending on the balance between the diffusiophoretic velocity (\mathbf{U}_{DP}) and convective drag (\mathbf{U}_{conv}). Utilizing the long-range diffusiophoretic exclusion phenomenon, here we conveyed a continuous water purification device as shown in Figure 4.1(c) and 4.1(d). The micro/nanofluidic device was fabricated using commercial Nafion sheets (cation-exchange medium) in the glass/PDMS building block. Two Nafion sheets were aligned on the glass slide to form a microchannel between the sheets. After the alignment, blank PDMS was irreversibly bonded on top of it. As the colloidal suspension passed through the microchannel, the diffusiophoretic exclusion was initiated by the formation of ion concentration boundary layer. The detailed fabrication steps and experimental setup were described in chapter 4.2. Through rigorous analysis of the ion concentration boundary layer, we verified that the Sherwood number was a key parameter to describe the natural ion depletion and diffusiophoretic exclusions in our continuous type purification platform. In the next

chapter, quantitative theoretical analysis and experimental confirmations of the ion concentration boundary layer formation were discussed.

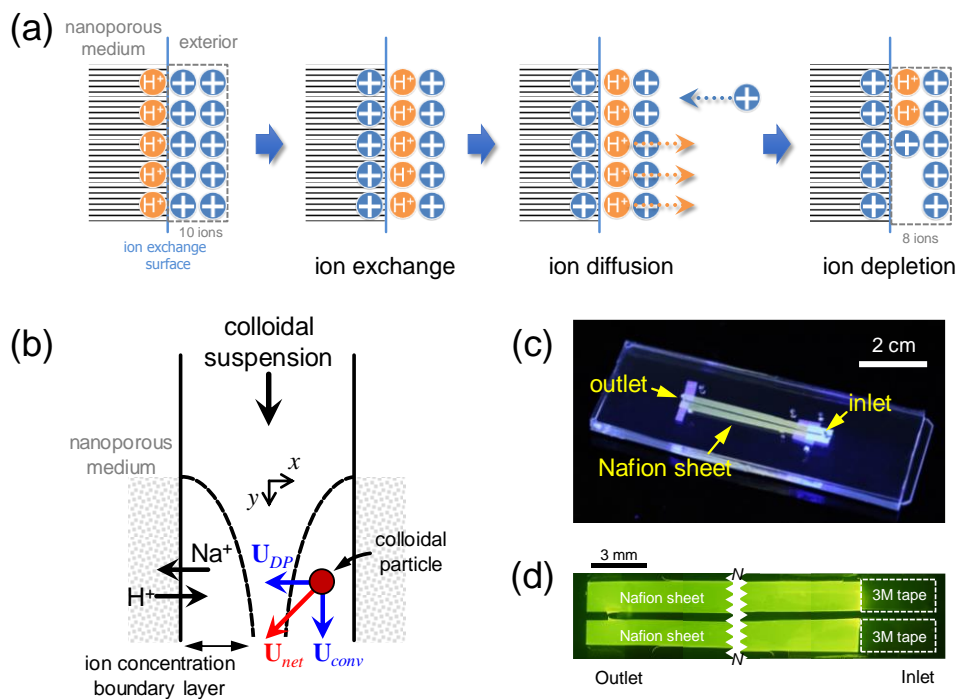


Figure 4.1. (a) The schematic diagram of natural ion depletion mechanism around nanoporous medium. This diagram is conceptual schematic to understand ion exchange and ion depletion process. (b) Schematic diagram for micro/nanofluidic device utilizing diffusiophoretic exclusion of colloidal particles induced by concentration gradient inside ion concentration boundary layer. The arrows on colloidal particle denote velocity components; U_{DP} is the diffusiophoretic velocity, U_{conv} is the convective drag by ambient flow of colloidal suspension and U_{net} is the net velocity of the colloidal particle. (c) photo of assembled device and (d) the microscopic image of it.

4.3.2 Boundary layer analysis

Florea *et al*[71] showed that four different ionic transport equations for Na^+ , Cl^- , H^+ and OH^- can be reduced into analytically tractable equations for the ionic pairs such as $\text{Na}^+\text{-Cl}^-$ and $\text{H}^+\text{-Cl}^-$, if the local electroneutrality and the chemical equilibrium of water are satisfied in the electrolyte. Similar to their approaches, we obtained following simplified governing equations from the fully-coupled model in Appendix C.

$$\frac{\partial c_{Na}}{\partial t} = -\nabla \cdot \left(-D_{eff} \nabla c_{Na} + c_{Na} \mathbf{u} \right) \quad (4.1)$$

$$\frac{\partial c_H}{\partial t} = -\nabla \cdot \left(-D_{Heff} \nabla c_H + c_H \mathbf{u} \right) \quad (4.2)$$

and

$$c_{Cl} = c_{Na} + c_H \quad (4.3)$$

where \mathbf{u} the flow field, c_i the concentration of species i , D_{eff} and D_{Heff} effective diffusivities as $D_{eff} = 2D_{Na}D_{Cl} / (D_{Na} + D_{Cl})$ and $D_{Heff} = 2D_H D_{Cl} / (D_H + D_{Cl})$. The boundary conditions were followed; (i) At inlet, $c_{Na} = c_0$ and $c_H = c_{H0}$ where c_0 is the bulk electrolyte concentration, c_{H0} is the bulk proton concentration. We assumed $\text{pH} = 7$ at the bulk in the theoretical works. (ii) At outlet, convective out flow condition such as $\mathbf{n} \cdot (-D_i \nabla c_i + c_i \mathbf{u}) = \mathbf{n} \cdot (c_i \mathbf{u})$ was applied for each i -th species where \mathbf{n} is the outward normal vector. (iii) At ion exchange surface, $c_{Na} = 0$ and $-\mathbf{n} \cdot (-D_H \nabla c_H + c_H \mathbf{u}) = -\mathbf{n} \cdot (-D_{Na} \nabla c_{Na} + c_{Na} \mathbf{u})$. Using the scaling analysis and non-dimensionalization, equation (4.1) became the following formula in the limit of steady state as

$$\frac{\partial^2 \tilde{c}_{Na}}{\partial \tilde{x}^2} - Sh \frac{\partial}{\partial \tilde{y}} \left(\tilde{c}_{Na} \tilde{u}_y \right) = 0 \quad (4.4)$$

where tilde symbol (\sim) means dimensionless variables whose characteristic scales were bulk concentration (c_0), the half-width of the microchannel (W), the longitudinal length (L_n) of the nanoporous medium, and the mean flow velocity (U_{mean}) for c_{Na} , x , y and u_y , respectively. Sh is the Sherwood number which is defined as the ratio of longitudinal convective transfer (y -direction in this work) and transverse diffusion rate (x -direction) as

$$Sh = \frac{W^2 U_{mean}}{L_n D_{eff}} \quad (4.5)$$

Therefore, this derivation revealed that Sh was the unified single parameter governing this continuous ion exchange process. Adjusting Sh , one would be able to determine the overlap condition of each Na^+ concentration boundary layer. When Sh was much smaller than 1, the second term in equation (4.4) became negligible relative to the first term. This implied that the transverse diffusive transport was more predominant than the longitudinal convection. Thus, the ion concentration boundary layers were overlapped in the case of $Sh \ll 1$. On the other hand, the boundary layers were independently formed when $Sh \gg 1$ (*i.e.* longitudinal convection was much greater than the transverse diffusion).

Usually, the Sherwood number has been utilized to characterize a mass transfer system where a boundary flux exists[89][91]. Although our dimensionless number seemed to resemble Peclet number, the boundary flux scale is included in our parameter. Sh in our system can be divided into $(W / L_n) \times (c_0 U_{mean}) / (D_{eff} c_0 / W)$. This notation implies (channel aspect ratio) \times (longitudinal convective transfer) / (boundary flux through ion exchange interface). In addition, even though the Peclet number connotes the ratio of convection and diffusion, the diffusion rate in the Peclet number does not always implies the diffusive flux through the ion exchange

interface. Therefore, Sherwood number was more appropriate to characterize our system rather than the Peclet number.

In order to demonstrate the intuitional insights related to Sh , only single concentration boundary layer was considered for convenience (*i.e.* left wall of the microchannel was assumed as the nanoporous medium while the right side was assumed as the impermeable surface). Based on the coordinate transform of $x = \xi - W$ and $y = \eta$, we suggested following concentration profile as the trial solution for equation (4.4).

$$c_{Na} = \begin{cases} c_0 \frac{\xi}{\delta} & \text{when } \xi < \delta \\ c_0 & \text{when } \xi \geq \delta \end{cases} \quad (4.6)$$

where δ is the thickness of the boundary layer as a function of η . Substituting equation (4.6) into equation (4.4) and integrating, we obtained the von Karman integral balance[89],

$$D_{eff} \left. \frac{\partial c_{Na}}{\partial \xi} \right|_{\xi=0} + \int_0^\delta u_\eta \frac{\partial c_{Na}}{\partial \eta} d\xi = 0. \quad (4.7)$$

Using the expression of the Poiseuille flow in slit (equation (C.5) in Appendix C) and the assumption of $\delta \ll W$, equation (4.7) became

$$\frac{D_{eff} c_0}{\delta} - \frac{U_{mean} c_0}{W} \delta \frac{d\delta}{d\eta} \approx 0 \quad (4.8)$$

which is a differential equation for the thickness of the boundary layer. Solving equation (4.8), we obtained the boundary layer thickness as a function of Sh as following

$$\frac{\delta}{W} \approx \left(\frac{3}{Sh} \frac{y}{L_n} \right)^{\frac{1}{3}} \quad (4.9)$$

From the equation (4.9) with linear superposition, the concentration boundary layers, which were generated from each porous medium surface, started to overlap when $Sh = 3$. One can expect that the boundary layer became thinner as Sh increased. This was because the formation of the layer was suppressed by the longitudinal convective transport with increasing Sh . As shown in the figure 4.2(a), the exclusion layer was directly visualized with various Sh . As Sh increased, the exclusion layer became thinner.

The flow rate of feed-stream was set to adjust Sh of the device in the actual experiments. Then the Na^+ concentration of the collected out-stream sample was analyzed using ion chromatography (DIONEX ICS-1100, ThermoFisher, USA). The results were shown in Figure 4.2(b) as a function of Sh . As Sh decreased, the Na^+ removal efficiency increased (*i.e.* lower Na^+ concentration at outlet) in both cases of 1 mM and 100 mM NaCl solution. Based on the definition of Sh , decreasing Sh would be accomplished by lowering sample flow rate, narrowing microchannel or lengthening porous medium. The experimental results of 1 mM NaCl (blue triangle in Figure 4.2(b)) was clearly matched with the theoretical prediction (solid line). The solid line indicates the theoretical calculation result of our model, whose description can be found in “Fully-coupled model for ion concentration boundary layer by ion exchange” in Appendix C. In spite of different geometry and injection flow rate between numerical domain and experimental device, the identical Sh results in the identical outlet concentration. This is because Sh was turned out to be a deterministic dimensionless number of our device from boundary layer analysis. Thus, at least in dilute NaCl concentration (1 mM in this work), the ‘quantitative’ comparison can be possible as shown in Figure 4.2(b). However, the results of 100 mM NaCl (red inverse-triangle in Figure 4.2(b)) were

deviated from the theoretical prediction. The deviation would be caused by the loss of ideal perm-selectivity at such high concentration and finite amount of H^+ in ion exchange medium. Since the external Na^+ was exchanged with internal H^+ , pH of out-stream should be altered. As shown in Figure 4.2(c), theoretical calculation (solid line) and pH measurement (inset of Figure 4.2(c)) directly indicated that the formation of ion concentration boundary layer strongly relied on the ion exchange process. Also, all experiments in Figure 4.2(b) and (c) were conducted within 5 – 200 minutes so that the effect of finite H^+ was negligible.

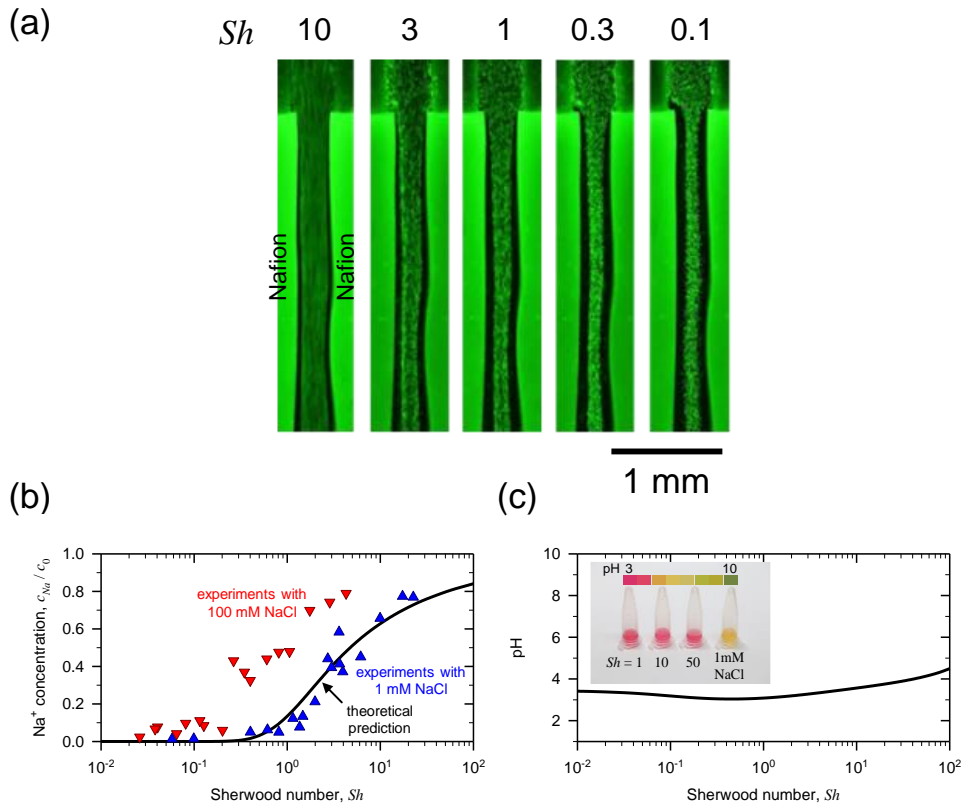


Figure 4.2. (a) Exclusion layer depending on Sh . (b) Normalized concentration of Na^+ at outlet as a function of Sh . Solid line was the theoretical prediction by the boundary layer analysis and symbols were the experimental results as labeled. (c) The prediction of out-stream pH as a function of Sh (Inset: Experimentally measured out-stream pH).

4.3.3 Continuous diffusiophoretic exclusion of colloidal particles

In this chapter, we discussed the elimination of the microscale substances from source water utilizing diffusiophoretic migrations induced by the concentration gradient inside the ion concentration boundary layer. As mentioned in the earlier chapters, the concentration gradient inside the boundary layer was enough to trigger the diffusiophoretic migration. In general, non-treated water contains various microscale toxic substances such as dust, microorganisms and waterborne pathogens. In order to eliminate such unacceptable matters, ultrafiltration, chemical or UV sterilization have been usually adopted[90, 91]. These conventional methods need high operation cost and large-scale infrastructures. Especially, the chemical sterilization would cause the environmental issues due to inevitable chemical byproducts. However, the method utilizing the diffusiophoresis we demonstrated relied on physical mechanisms so that none of the toxic byproducts was produced.

Figure 4.3 showed the diffusiophoretic exclusions of artificial microspheres and pathogens (*Escherichia coli* W3110 ATCC 27325 and *Salmonella enterica subsp. enterica serovar typhimurium* ATCC 19585, the preparation method of pathogens were discussed in Appendix section A) at $Sh = 10$ and 0.1 , respectively.

The images of $Sh = 0.1$ were taken firstly and the images of $Sh = 10$ were taken just after the first images. The time variations of two images were less than 5 minutes. Even though Nafion sheets owns only finite time, this time differences won't affect the reliability of the images. If the immersed particle possessed higher zeta potential (ζ_p), it would be excluded further away from the ion exchange medium. Due to the balance between the diffusiophoretic migration and the convective transport by longitudinal feed-streams, the charged particles were excluded from the ion exchange walls and tended to be focused at the channel center (the excluded

region was denoted as exclusion layer). Similar to the ion concentration boundary layer, the exclusion layer became thicker along the longitudinal direction (*i.e.* y -direction). However, when $Sh < 1$ (Figure 4.3(b) second column), the overlapped boundary layer resulted in diminishing concentration gradient in transverse direction (*i.e.* x -direction) so that the focused stream was broaden because of the Brownian motion of the micro particle. If we install the branched microstructure at the end of microchannel to selectively extract the sample only from the exclusion layers, water purification can be achieved based on this diffusiophoretic mechanism.

Firstly, we conducted the experiment without ion exchange phenomenon by installing only 3M tape (denoted as “w/o Nafion”) which is impermeable material. In this case, the particles were evenly distributed along the longitudinal direction, confirming that the present exclusion phenomenon was unrelated to the inertial focusing[92, 93]. Triggering ion exchange by installed Nafion sheets, the exclusion layers were successfully developed in an arc-shape along the microchannel as similar to the ion concentration boundary layers. The lower Sh resulted in the thicker exclusion layer. The inlet flow rate would be around 14 $\mu\text{L}/\text{min}$ at $Sh = 3$ with the presented device (cross sectional area was 0.4 mm \times 0.175 mm to 0.8 mm \times 0.175 mm). The contaminant-excluded water would be extracted at outlet with the flow rate of 5.3 $\mu\text{L}/\text{min}$. If multiple microchannels of diffusiophoretic exclusion are integrated, the purification throughput per unit system volume becomes 288 L/min/m³ which is comparable to other on-chip purification methods. The purification throughput of electrodialysis was 4.17 – 167 L/min/m³[54] and capacitive deionization was 138.9 – 1389 L/min/m³[94].

The exclusion of pathogens, *E. coli* and *S. typhimurium* were presented in the same figures. While *E. coli* was excluded as we expected, the concentration gradient inside the boundary layer unaffected *S. typhimurium*. This was because the zeta potential of *E. coli* is approximately three-times higher than that of *S. typhimurium*[95] so that the diffusiophoresis of *S. typhimurium* was too weak to initiate the formation of exclusion layer. Note that the microspheres has the highest zeta potential among the demonstrations. Its corresponding thicknesses of exclusion layer were the largest, confirming the simulation results that the higher zeta potential induced thicker exclusion layer. Interestingly, both *E. coli* and *S. typhimurium* were undetected in out-stream for the case of $Sh = 0.1$. In this case, the condition would provide a harsh environment (*i.e.* low pH) for the pathogen of weak acidic tolerance[96] so that one was able to expect the disinfection process happened without any chemical additive. Assisting these anomalous results, we conducted further experiment and simulation. First of all, we monitored the fluorescent signal of the pathogens under various pH conditions (pH 5, 4 and 3) as shown in Figure 4.4(a). The PDMS microchannel used in this experiment was fabricated by conventional PDMS fabricated steps[45] and had 200 μm width x 100 μm depth x 3 cm length. The gradual disappearance of the fluorescence with lower pH can be observed, but this cannot guarantee the inviability of pathogens. It has been reported that the signal of green fluorescent protein (GFP) gradually diminishes below pH 7 and GFP totally loses its fluorescent property below pH 4[97]. In order to confirm the assertion about disinfection induced by ion exchange process, we carried out acid resistance assay for each pathogen. See Appendix B for Detail information related to acid resistance assay. As shown in Figure 4.4(b), the survival percent of pathogens rapidly decreased below pH 5. These assay

results implied that the proposed disinfection can be achieved if low pH environment is generated inside ion exchange channel. pH in adjacent to the cation-exchange medium became around 3 so that one was able to expect the disinfection of the suspended pathogens. However, in the case of high Sh , the retention time of pathogens in our channel could not be sufficient to disinfect due to the high injection rate at inlet. This is why the diffusiophoretic exclusion was observed in $Sh = 10$ as shown in Figure 4.3(a). While our experiments suggested the possibility of pathogen disinfection, Cheng and Moraru[98] has reported the diffusiophoretic exclusion of bacteria. This discrepant result came from the presence of biological buffer. Cheng and Moraru employed a phosphate buffer so that the harsh pH environment in adjacent of Nafion diminished, leading to the diffusiophoretic exclusion. However, in our system, the absence of buffer reaction in electrolyte domain resulted in the harsh pH environment enough to disinfect the pathogen.

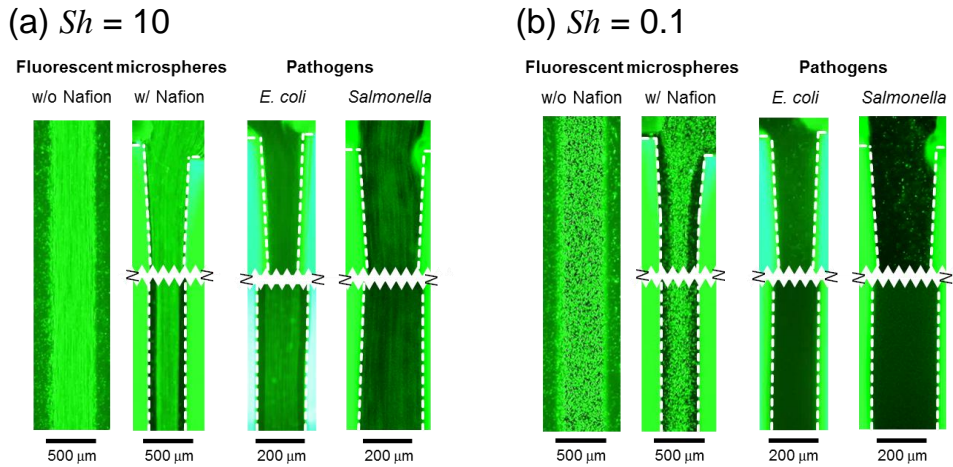


Figure 4.3. Diffusiophoretic exclusion layer of artificial microsphere (1 μm polystyrene) and pathogens (*E. coli* and *S. typhimurium*) with $Sh = 10$ (a) and $Sh = 0.1$ (b) respectively.

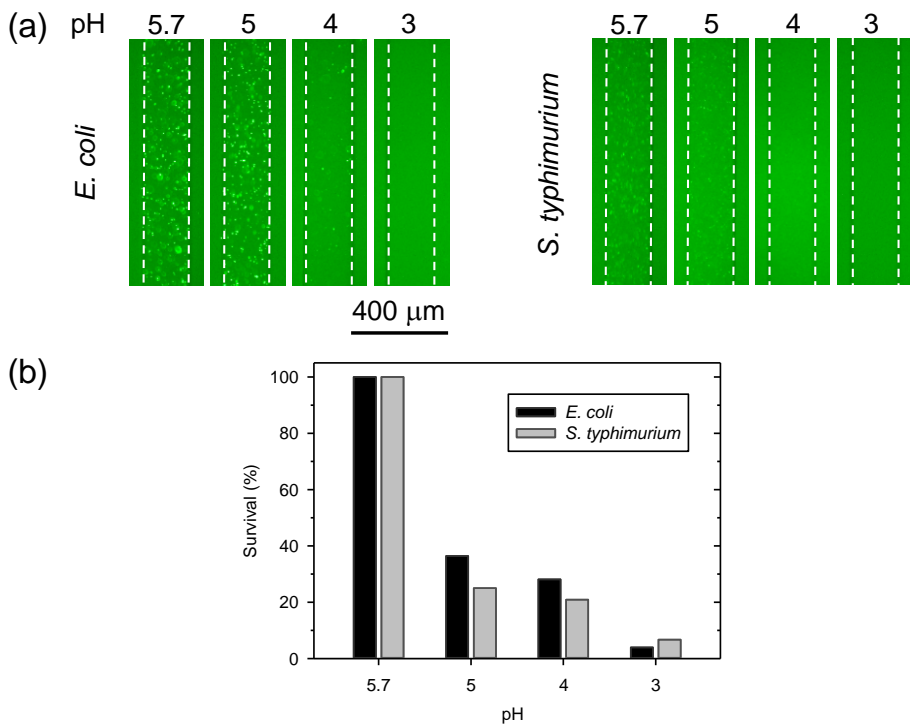


Figure 4.4. (a) Microscopic images showing decrement of pathogen fluorescent signal with low pH. (b) % survival of pathogen under various pH obtained from acid resistance assay.

4.3.4 Long-time ion exchange to obtain actual sustainable time.

Note that the diffusiophoretic exclusion, such as the particle-free zone in Figure 4.3, stopped after the internal protons were completely consumed, resulting the collapse of the ion concentration boundary layer. In other words, the ion exchange and the diffusiophoretic exclusion processes were impermanent so that our system possessed finite sustainable time. The requirements for the sustainable exclusion are (i) highly charged medium, (ii) large membrane width or volume and (iii) low Sh . In order to obtain the actual sustainable time, additional long-time experiment was conducted with 10 mM NaCl and $Sh = 10$

In order to obtain the actual sustainable time, additional long-time experiment was conducted with 10 mM NaCl and $Sh = 10$ as shown in Figure 4.5(a). The thickness of the exclusion layer was measured at ~2.3 mm from the starting point of Nafion after injection flow reached the steady state (~10 minutes). Negligible swelling and shrinking of Nafion were observed in the long-time operation. Adherence of colloidal particles to the glass substrate and photo bleaching of Nafion sheets were observed during the experiment. Asymmetric exclusion layers at each time were caused by leakage flow through the gap of Nafion/PDMS or Nafion/glass. However, the asymmetry was not critical to measure the layer thickness as a function of time. The exclusion layer was quantitatively measured in 5 different devices as shown in Figure 4.5(b). The exclusion phenomenon was actually sustained over 8 hours. By linear extrapolation, we expected that the exclusion would be terminated after 18 hours

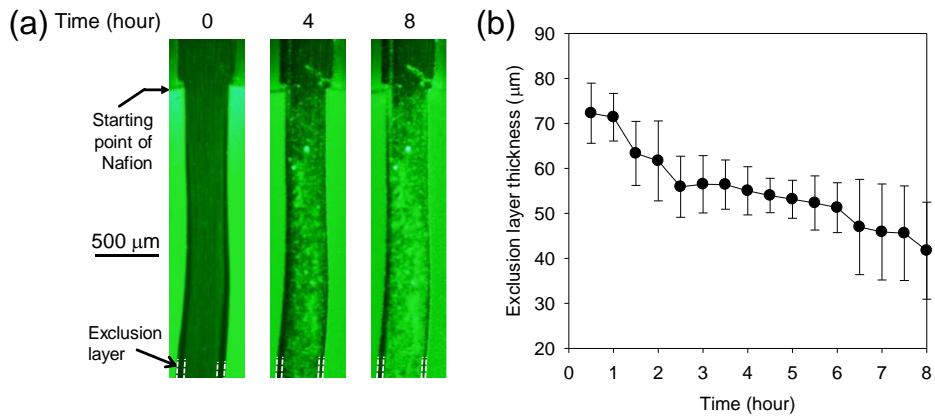


Figure 4.5. Long-time operation on micro/nanofluidic ion exchange device. (a) Time-revolving snapshots of exclusion layer and (b) the thickness of exclusion layer as a function of time.

4.4. Conclusions

In this chapter, we investigated the concentration gradient-induced diffusiophoretic migration inside the ion concentration boundary layer formed nearby the ion exchange material. From the previous research[71], the ion exchange leads to the natural ion depletion around the material so that the ion concentration boundary layer would be generated and the concentration gradient inside the layer results in anomalous long-range particle exclusion away from the ion exchange interface. In order to utilize the exclusion phenomenon for micro/nanofluidic water purification platform, here we established a continuous type of ion exchange device. Through the rigorous boundary layer analysis, the layer was quantitatively characterized by using a single parameter Sherwood number (Sh) which is a dimensionless number containing external flow rate, diffusivity of dissolved ionic species and geometrical factors. Depending on Sh , we experimentally (artificial microsphere and pathogens) demonstrated that the long-range diffusiophoretic exclusion can be applicable to the continuous water purification. Our diffusiophoretic platform would provide the economic, high energy-efficient and portable water purification as well as conventional use of ion exchange process such as desalination or water softening.

Chapter 5. Experimental Investigation

on Spatiotemporal Concentration Profile

of the Ion Concentration Polarization Layer

5.1 Introduction

Ion concentration polarization (ICP) is a fundamental electrokinetic phenomenon that occurs near a perm-selective nanoporous membrane or nanochannel. Concentration gradients are induced by the applied dc bias next to the perm-selective membrane. These concentration gradient regions are called ion depletion zone (low concentration) and ion enrichment zone (high concentration) which is formed at the anodic and cathodic side, respectively. This is the case of cation-selective membrane (*e.g.* Nafion) and *vice versa*.

However, the exact solution of ICP phenomenon is still lacking because of the high complexity of the phenomenon which includes highly coupled physical parameters such as dynamic evolution of electric field, nonlinear fluid flow, charged species transport and wide range of physical scale ranging from nanometers to centimeters. Because of this high complexity, the experimental and theoretical investigation of componential problems of ICP can lead the in-depth understanding of ICP such as nonlinear electrokinetic flow[17, 34], amplified electric field[22], electroconvection[18], micro–nanofluidic ion transport[99], and so on.

One of the key characteristic of ICP is that charged particles being repelled from the ion depletion zone which acted as a virtual barriers. With the balance of hydrodynamic drag force and electrophoretic force on the charged molecules, ICP

had been widely applied to a preconcentrator for the detection of low abundant molecules. Continuous type ICP device with diverse target molecules had been reported due to its easy operation and a factor up to million-fold[19, 43, 100-103]

Fundamental study on preconcentration dynamics of ICP and engineering applications can be explored based on the concentration profile. The concentration profile of diffusion layer was predicted to be linear in the early stage of ICP model. Classically, the model only considered diffusion and electro-migration as the mechanism of ion transportation based on Nernst-Planck equation[16]. Only Ohmic and limiting ionic current could be explained with this early model (Figure 5.1(a)). With more theoretical and experimental research, people verified that convection effect should also be considered into the model. Strong vortices generated by non-linear electrokinetic fluid slip efficiently mixed the electrolyte of the depletion zone making the concentration of depletion zone nearly flat and below 10% of bulk concentration[17, 49, 56, 104]. The mechanism of overlimiting current regime was verified which was followed by Ohmic and limiting current regimes (Figure 5.1(b)). Once again the model was improved including multiple vortexes induced by primary vortex. Step-wise concentration profile in the ICP layer was verified with an in-depth experimental investigation of multiple vortical instabilities inside the ICP layer[55] (Figure 5.1(c)). Most of the research focused on ion depletion zone which had rather low concentration compare to the bulk concentration ($< 0.1 c_0$).

In this work, in-depth experimental investigation on spatiotemporal concentration profile of diffusion-convection layer during ICP process was examined. Here, diffusion-convection layer was defined as the intermediate region between bulk region and ion depletion zone. Unlike the traditional diffusion-

convection layer which had almost linear diffusion layer, the measured data indicated near plateau concentration distribution over the diffusion-convection layer in a microfluidic environment (Figure 5.1(d)). The propagating plateau concentration profile with nearly 60 % of bulk concentration was confirmed with visualization through fluorescent dye and microelectrode conductivity measurements, respectively. Also, three experimental parameters (fluorescent dye, bulk concentration and initial volumetric flow) were investigated to broaden the knowledge related to this phenomenon.

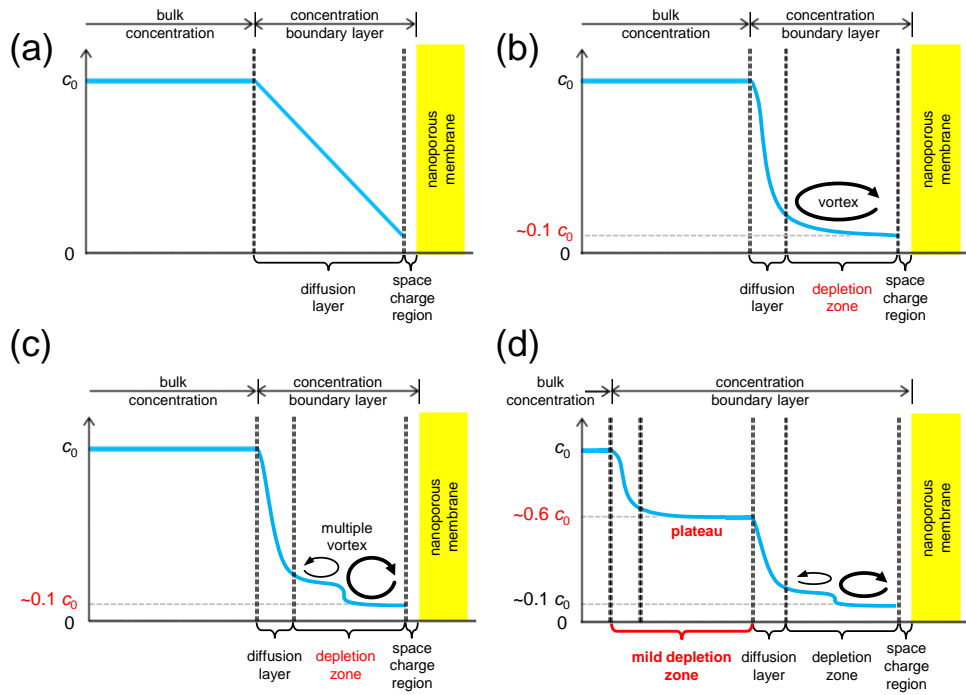


Figure 5.1. Schematic diagrams of the concentration profile of ICP layer. (a) Initial model of ICP layer with diffusion and drift considered. (b) Non-linear electrokinetic fluid slip induced vortex was added to (a). (c) Multiple vortex caused by primary vortex was added to (b). (d) Proposed model including plateau concentration next to diffusion layer.

5.2. Experimental Setup

5.2.1 Device Fabrication

The microelectrodes were patterned on a glass wafer using a standard photolithography, deposition and lift-off process[22, 31, 55]. First, typical SPM cleaning was performed on the glass wafer. Then the glass wafer was baked at 110 °C for 5 minutes for dehydration. AZ 5214E photo resister was sufficiently dispensed on the substrate. The substrate was spun at 500 rpm for 5 seconds with acceleration of 100 rpm/s and at 4000 rpm for 40 seconds with acceleration of 1000 rpm/s using spin coater to form 1.4 μm depth of AZ 5214E. The substrate was prebaked at 110 °C for 50 seconds and was exposed to 75 mJ/cm^2 of UV with the mask on MA6. Reversal bake was performed to the substrate at 120 °C for 2 minutes. Flood exposure of $> 200 \text{ mJ}/\text{cm}^2$ was dosed. Afterwards substrate was immersed into the developer AZ 300 MIF for 45 seconds and was immersed into deionized water for 30 seconds. Then postbake was performed to the substrate at 120 °C for 50 seconds.

10 nm titanium and 100 nm gold were deposited on the glass wafer using E-Gun evaporator where titanium acted as an adhesion layer. Afterwards unnecessary titanium-gold layer was removed by metal lift-off process. Glass petri dish was filled with acetone and was covered with silver foil to prevent evaporation. The gold deposited glass wafer was immersed into the acetone and was agitated with sonicator for 30 minutes. The wafer was sprayed with isopropanol, ethanol, and deionized water around 10 seconds consecutively and was dried with air gun. After the lift-off process the wafer was diced into proper size with dicing saw. As a result, glass wafer containing microelectrodes patterns (50 μm width, 200 μm spacing)

was fabricated as shown in Figure 5.2(a). Local potentials was measured using Au μ -electrodes. Perm-selective nanoporous membrane (Nafion, 20 w.t. % resin, Sigma Aldrich, USA) was patterned on the sliced glass wafer with Au μ -electrodes using surface patterning method. The Nafion (width 200 μm , depth $\sim 1 \mu\text{m}$) was positioned 500 μm away from the patterned microelectrodes as shown in Figure 5.2(b).

Polydimethyl siloxane (PDMS, Sylgard 184 Silicone elastomer kit, Dow Corning) based microchannel (width 200 μm , depth 15 μm) molding was fabricated using previously published methods[53, 105]. The PDMS molding was irreversibly bonded on top of the Nafion patterned substrate using plasma bonder (Cute-MP, Femto Science, Korea). Two microchannels were connected by Nafion allowing micro-nano-micro hybrid device, as shown in Figure 5.2(b). Sliced glass wafer (1.75 cm x 3.5 cm) was bonded on top of the slide glass (2.5 cm x 7.5 cm) with clear super glue. Wires were electrically connected to each Au μ -electrodes with silver conductive epoxy adhesive (8331, MG Chemical).

5.2.2 Device operation

Figure 5.2(c) shows the operating platform of the device for the visualization and concentration profiling experiments. Electrolyte solution of KCl (0.1 mM ~ 10 mM, Sigma-Aldrich, USA) mixed with 20 μm fluorescent dye (Alexa 488, Invitrogen, USA) and carboxylate-modified FluoSpheres ($d = 1 \mu\text{m}$, yellow-green fluorescent, Invitrogen, USA) was injected into the main microchannel. Also, KCl electrolyte (10 mM ~ 1 M) at least 100 times higher than main microchannel was injected to the buffer microchannel which was mixed with 20 μm Alexa 488. The high KCl concentration at the buffer microchannel were to minimize a voltage drop in the buffer solution and to minimize the unnecessary effect of concentration change of ion enrichment zone[33, 41].

An inverted fluorescence microscope (IX53, Olympus, Japan), CCD camera (DP73, Olympus, Japan) and commercial software (CellSense, Olympus) were used to image and detect the electrokinetic flow inside the microchannel. The fluorescent intensity of the images were analyzed by ImageJ (NIH, Bethesda, MD, USA) to calculate the fluorescent concentration. The initial volumetric flow was formed by the height differences of the reservoirs if necessary. Voltage was applied with source measure unit (Keithley 236, USA) while current-time responses were obtained by Ag/AgCl electrodes simultaneously. The applied voltage was in the regime of overlimiting regime[37] causing ICP phenomenon near the nanoporous membrane. Also, other four source measure units (Keithley 236, 237, 238, USA) measured the local potentials of the microchannel simultaneously with patterned Au microelectrodes. Since there were 7 patterned Au microelectrodes and 4 measuring units, only 4 local potentials were measured at each experiments. The

current and local potentials were measured automatically using Labview program (National Instruments, USA).

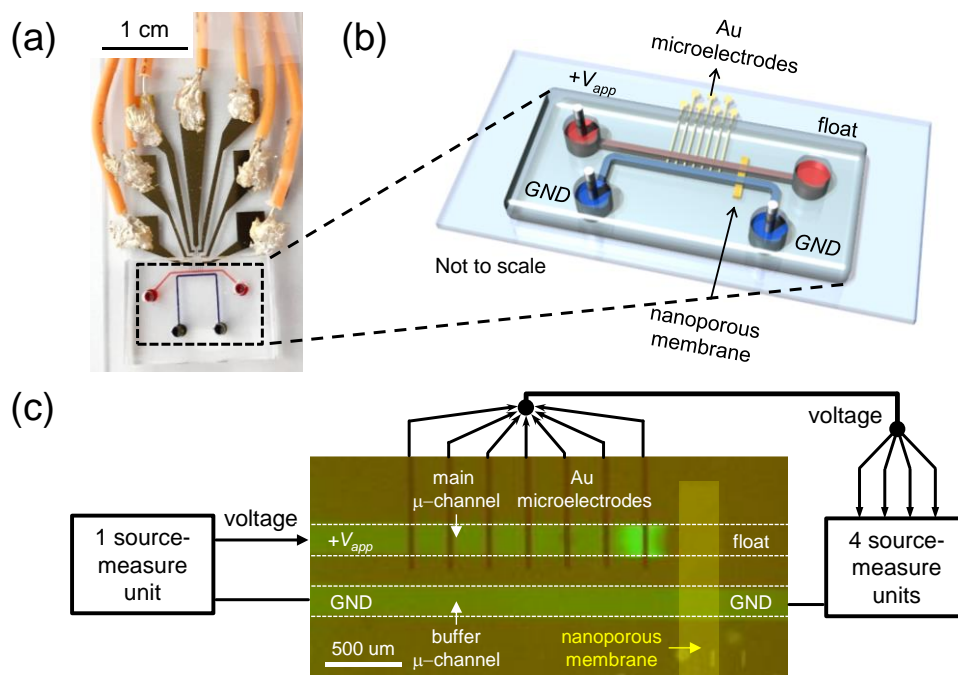


Figure 5.2. (a) Snapshot of the fabricated device containing Au μ -electrodes. The device was fabricated with conventional soft lithography method and lift-off process (b) 3-D schematic of the device showing the applied potential of each reservoirs and Au μ -electrodes measure the local potential. (c) Schematic figure of operating platform with microscopic view of the fabricated device.

5.2.3 In situ concentration measurement

The average conductivity of the electrolyte between each microelectrodes σ was calculated by the Ohm's law $\sigma = i / (|\Delta V| / L * A)$, where i is the current passing through the Nafion junction and ΔV is the voltage difference between microelectrodes. L (250 μm or 500 μm) was a gap between the microelectrodes and A (14.5 mm X 200 mm) was the cross-sectional area of the microchannel. The local concentration was estimated by reference conductivity of the KCl solutions. The reference conductivity in 0.01, 0.1, 1, 10, 100 mM KCl electrolyte were $\sim 1.61 \mu\text{S cm}^{-1}$, $\sim 14.5 \mu\text{S cm}^{-1}$, $\sim 150 \mu\text{S cm}^{-1}$, 1.43 mS cm^{-1} , 13.0 mS cm^{-1} respectively[55]. Based on these sets of conductivity values, the measured local average conductivities were converted into local average concentration values.

5.3. Results and discussion

5.3.1 Unexpected plateau concentration region

Figure 5.3(a) shows the time evolving snapshots of the main microchannel with the applied voltage ($+V_{\text{app}} = 70 \text{ V}$). The main microchannel was filled with 10 mM KCl (c_0) as a background electrolyte, while buffer microchannel was filled with 1 M KCl. With the applied voltage, ion depletion zone was formed next to the nanoporous membrane and fluorescent intensity was increased due to the pre-concentrated fluorescent dyes. Four microelectrodes with odd-numbered position which had 500 μm gap were used to measure the local potentials of the solution in this section.

The region of interest was the pre-concentrated fluorescent dye region which propagated toward the anode indicated as the sky blue arrow in Figure 5.3(a). Red (c_{13}), yellow (c_{35}) and green (c_{57}) rectangular region in Figure 5.3(a) were the average and spatiotemporal concentrations between the electrodes were shown in Figure 5.3(b). To be more specific, explanation of red rectangular (c_{13}) region was followed. Between 0 ~ 1 minute, fluorescent intensity was the same as initial condition of mixed solution and the local average concentration (c_{13}) was measured to be 10 mM (0 ~ 1 min red circles in Figure 5.3(b)). Between 1 ~ 2 minutes, increased fluorescent intensity region propagated toward the left side of red rectangle and the local average concentration went down reaching ~6 mM (1 ~ 2 min red circles in in Figure 5.3(b)) at the same time. After 2 minutes, increased fluorescent intensity was fixed and also the local average concentration was fixed from 6 mM (2 ~ 5 min red circles in Figure 5.3(b)). This explanation can also be applied to other regions; yellow (c_{35}) and green (c_{57}) rectangular regions. As a

results, the concentration of increased fluorescent dye regions was verified to be $\sim 0.6 c_0$ based on the visualization and calculated data. Unlike traditional models, the unexpected long plateau concentration profile was observed which propagated toward the anode (sky blue arrow region in Figure 5.3(b)).

Also, the time when c_{13} reached plateau concentration (~ 6 mM) was similar to the time when c_{35} started to decrease ($t = \sim 2$ min) and the time when c_{35} reached plateau concentration (~ 6 mM) was similar to the time when c_{57} started to decrease ($t = \sim 3$ min). One can infer that the concentration boundary was passing through the specific electrodes at those times. Also, $1 \mu\text{m}$ FluoSpheres were being repelled at the boundary of bulk concentration and were being preconcentrated in this experiment.

Even though we experimentally demonstrated the plateau concentration phenomenon, theoretical and simulation results are still lacking to explain the fundamental physics. So, various experiments were conducted to broaden our knowledge related to this phenomenon.

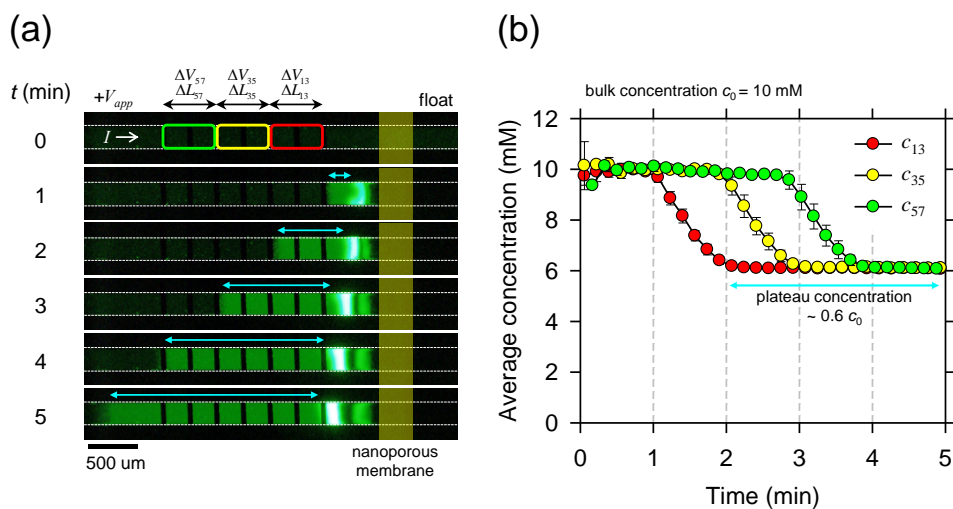


Figure 5.3. (a) Microscopic view of time-evolving snapshots of the main microchannel with 10 mM KCl (c_0) as background electrolyte. Preconcentrated fluorescent dye were being propagated toward the anode. The region between two measured electrodes were indicated as red (c_{13}), yellow (c_{35}) and green (c_{57}) rectangles. Also, plateau concentration region was indicated as sky blue arrow. (b) Corresponding local average concentration vs. time responses of c_{13} , c_{35} and c_{57} . Each region reached plateau concentration ($\sim 0.6 c_0$) when the propagating fluorescent dye reached the left side of rectangle, respectively.

5.3.2 Experimental parameter sweep

5.3.2.1 Influence of fluorescent dye on plateau concentration

Along with cationic fluorescence dye (R6G), Alexa 488 had been widely used to visualize ICP near the permselective nanochannel and nanoporous membrane [30, 41, 106, 107]. As mentioned earlier, pre-concentrated Alexa 488 fluorescent dye was able to visualize the plateau concentration region, however it might affect the formation of plateau concentration region. To examine the influence of fluorescent dye on plateau concentration, the same experiment was conducted as in section 5.3.1 but without fluorescent dye.

First, calculated local average concentration showed the same plateau concentration profile ($\sim 0.6 c_0$) even without the fluorescent dye as shown in Figure 5.4. Here, the data was more unstable than in the previous section because the voltage difference between the electrodes was smaller.

Second, carboxylate-modified $1 \mu\text{m}$ microparticles were being repelled and pre-concentrated from the specific propagating boundary. This was the same phenomenon observed in section 5.3.1 with fluorescent dye.

Lastly, the concentration of the fluorescent dye was significantly smaller than those of the buffer ions in section 5.3.1. It is known that the fluorescent intensity is proportional to fluorescent dye concentration when fluorescent intensity is rather small [20, 108]. At the plateau concentration region, fluorescent dye concentration was calculated as $90 \mu\text{M}$ ($20 \mu\text{M} \times 450\%$) while the buffer ions concentration was calculated to be 6mM ($10 \text{mM} \times 60\%$). Based on the measured data one can calculate the contribution of each ion species to the overall current. Their contribution is proportional to the electrical mobility and concentrations. The

contribution of Alexa 488 was calculated to be only 0.68% ($\mu_{\text{Alexa488}}C_{\text{Alexa488}}/\mu_{\text{Cl}}C_{\text{Cl}}$) compared to the anion ions. Here, the electrical mobilities of Alexa488 and Cl^- were $\mu_{\text{Alexa488}}=36.0\times 10^{-9}$ and $\mu_{\text{Cl}}=79.1\times 10^{-9}$ m^2/Vs , respectively. Also, Alexa488 is pH-independent between the pH values of 4 and 10[109].

Based on the three experimental results mentioned, the influence of fluorescent dye was turned out to be negligible but can visualize the plateau concentration region. Also, the fluorescent intensity wasn't inversely proportioned to the local electrolyte concentration[56] in this experiment, and since the plateau concentration region owned similar concentration ($\sim 0.6 c_0$) it had same physical properties such as electric field, conductivity, flow field and so on, at the specific moment.

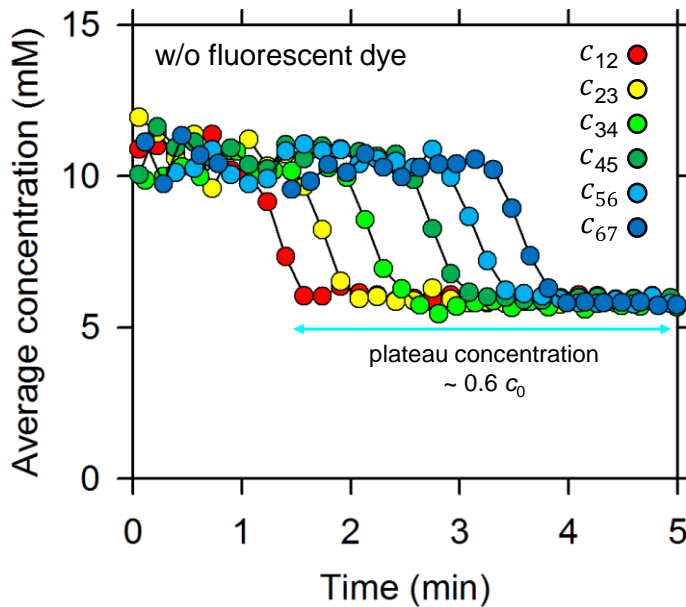


Figure 5.4. Local average concentration vs. time responses without fluorescent dye. After each region reached plateau concentration ($\sim 0.6 c_0$) the local average concentration was fixed. All seven μ -electrodes were used in this experiment.

5.3.2.2 Bulk concentration vs. plateau concentration (%)

The next parameter that we examined was the initial bulk concentration's influence on plateau concentration phenomenon. Initial bulk concentration was changed ranging from 0.1 mM to 10 mM. As shown in Figure 5.5(a), the plateau concentration phenomenon occurred at every concentration ranging from 0.1 mM to 10 mM. Also, the percentage of plateau concentration to bulk concentration was nearly 60% of bulk concentration. However, the percentage slightly increased as the bulk concentration became higher. To be more specific, percentage of plateau concentration to bulk concentration of 0.185 mM and 1.03 mM were 56.5% and 59% respectively. At the same time, the time required to reach the plateau concentration increased as the bulk concentration increased as shown in Figure 5.5(b). Since plateau concentration phenomenon was observed independently from the bulk concentration, joule heating effect was eliminated from the potential cause of plateau concentration[110].

The reason why higher concentrations above 10 mM such as 100 mM or 1000 mM were missing was because of the unstable ion depletion zone. At high concentration, the current mechanism changed from electro-osmotic flow to electro-osmotic instability[37]. In the electro-osmotic instability regime, ionic current and local potential oscillated too fast hindering the measurement of concentration profile (See Figure 5.6)). However, the propagating pre-concentrated fluorescent region was observed along the microchannel even at high concentration region. So, one can deduce that plateau concentration phenomenon occurs at every bulk concentration.

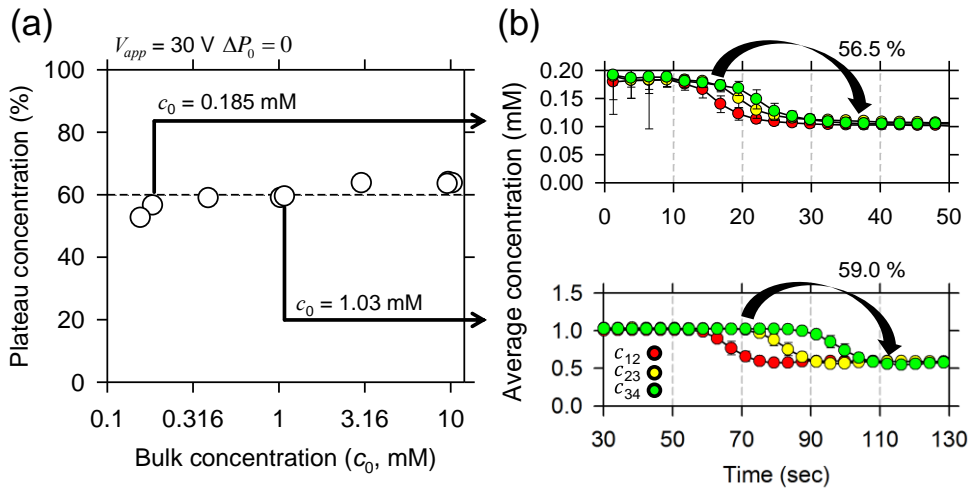


Figure 5.5. (a) Initial bulk concentration vs. percentage of plateau concentration to bulk concentration ($\sim 0.6 c_0$). The plateau concentration phenomenon occurred at every concentration. (b) Local average concentration vs. time responses of two different bulk concentration 0.185 mM and 1.03 mM.

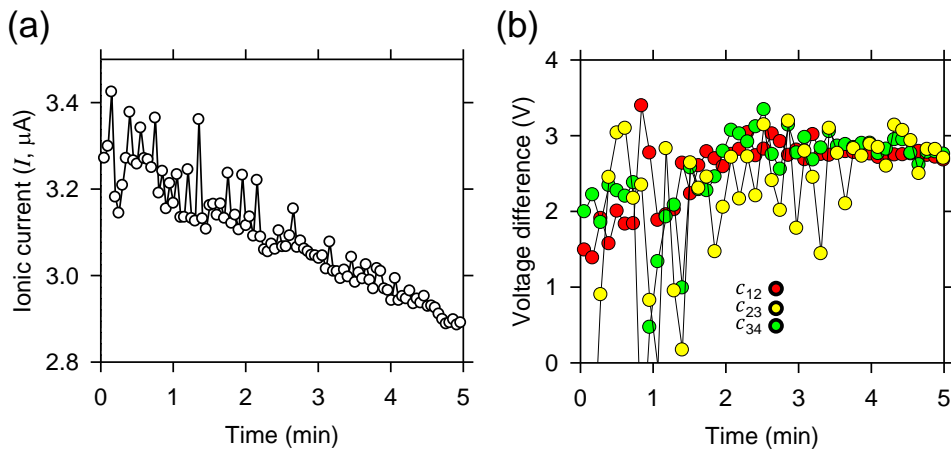


Figure 5.6. Unstable measured data at high bulk concentration ($c_0=20$ mM) due to unstable ion depletion zone at electro-osmotic instability regime. (a) Unstable current-time responses and (b) unstable voltage difference between electrodes hindered the measurement of local average concentration.

5.3.2.3 Influence of initial volumetric flow on plateau concentration

Lastly, initial volumetric flow effect on plateau concentration was examined. Many microfluidic applications utilized initial volumetric flow to increase the efficiency of preconcentration[53, 92, 111]. Also, initial volumetric flow is one of the key parameter influencing the formation of ICP[111, 112]. The propagation velocities of plateau concentration were $5.1 \mu\text{m/s}$ and $8.4 \mu\text{m/s}$ with and without initial volumetric flow, respectively. Also, the concentrations of fluorescent dye at the plateau concentration were calculated as $50 \mu\text{M}$ ($20 \mu\text{M} \times 250 \%$) and $72 \mu\text{M}$ ($20 \mu\text{M} \times 360 \%$) with and without initial volumetric flow, respectively. The data showed that the propagation velocity of plateau concentration decreased while concentrations of fluorescent dye increased with higher initial volumetric flow. This results agreed with the suppressed ICP which initial volumetric flow affects the formation of ion depletion zone. Also, the percentages of plateau concentration to bulk concentration were 60% and 57% which was similar with and without the initial volumetric flow, respectively as shown in Figure 5.6. As a result, we deduced that even though initial volumetric flow affects the formation of plateau concentration region it doesn't influence the percentage of plateau concentration to bulk concentration.

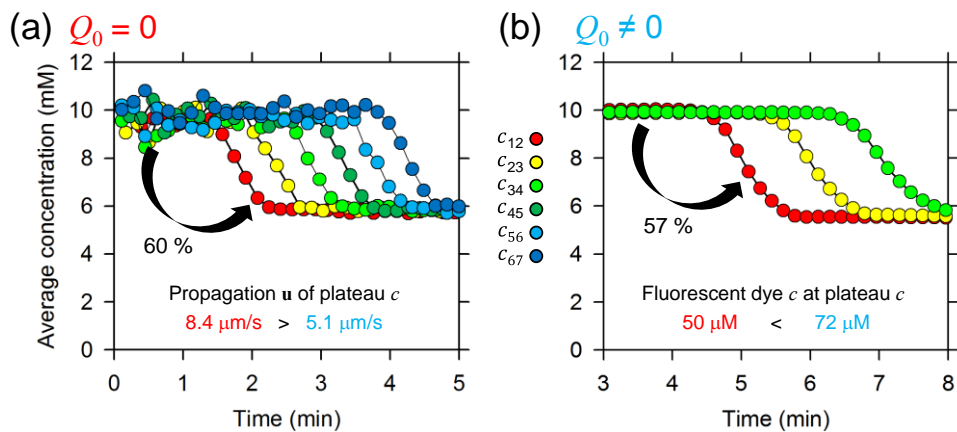


Figure 5.6. Local average concentration vs. time responses (a) without initial volumetric flow and (b) with initial volumetric flow. The percentages of plateau concentrations to bulk concentration were similar.

5.3.2.4 Rightness of *In situ* concentration measurement with Au microelectrodes

As mentioned in the earlier section, the local ion concentrations were estimated with Au microelectrodes arrays as shown in Figure 5.2. When using microelectrodes array there are several effects to be considered such as Joule heating[110], faradaic reaction[113, 114], induced charge electrokinetic effects[115, 116], *etc.*

First, Joule heating effect is highly dependent on electrolyte concentration so it can be neglect based on the fact that the plateau concentration occurred at every bulk concentration which was mentioned at section 3.2.2.

Next, the interfacial potential difference between bipolar electrode and solution is highest at the ends of the electrode[114]. So faradaic processes are always observed there first. Based on our experimental settings, the maximum potential difference within single electrode was calculated to be 0.28 V while the required potential difference of water splitting was 1.23 V. This was due to the rather high concentration of plateau concentration region which was nearly 60 % of bulk concentration. The voltage was applied to the rather low ion depletion zone not on the plateau concentration region. Since the maximum potential difference was rather smaller than 1.23 V faradaic reaction and electrokinetic effects were small enough in our experiments.

Above all, the estimated ion concentrations using microelectrodes were similar to those ion concentrations we had used. For example, the error was less than 4 % when 10 mM KCl electrolyte was used.

5.4. Conclusions

In this work, spatiotemporal concentration profile of diffusion-convection layer during ICP process had been measured with patterned microelectrode. Unlike the traditional diffusion-convection layer which had linear concentration profile, the measured data showed near plateau concentration distribution over the diffusion-convection layer in a microfluidic environment.

The propagating plateau concentration profile with nearly 60 % of bulk concentration was confirmed with fluorescent dye visualization and microelectrode conductivity measurements, respectively. Also, three experimental parameters (fluorescent dye, bulk concentration and initial volumetric flow) were investigated to broaden the knowledge of plateau concentration.

To the best of our knowledge, this was the first time that plateau concentration region was demonstrated experimentally at ICP layer. Until now people mainly focused on the ion depletion zone ($<0.1 c_0$) which had rather low concentration due to its distinct properties. However, even though plateau concentration region had rather higher concentration ($\sim 0.6 c_0$) compare to ion depletion zone, it also acted as a distinct boundary to the movement of charged molecules as well.

This anomalous concentration profile can provide a key information to the fundamental study on preconcentration dynamics of ICP and novel engineering applications utilizing micro-nanofluidic system.

Chapter 6. Conclusion

In this thesis, concentration boundary layer's physical properties were discussed. The mechanism of concentration boundary layer induced by permselective ion transport was divided into two parts; electromigratory flux and diffusive flux. We adopted physical phenomenon called ICP and diffusiophoresis in electromigratory flux and diffusive flux, respectively. First, an air valve using Young-Laplace equation was conceived for exact electrokinetic measurement with convenient experiments. Secondly, parallel formation of nanoporous membrane with the microchannel having the effect of enhancing surface conduction lead to the alternation ionic transportation mechanism from electroosmotic flow to surface conduction. The change of mechanism gave a unique property of stabilizing concentration boundary layer propagation even at high concentration electrolyte due to newly formed bifurcated current path. Also, non-destructive cellular preconcentrator was demonstrated using this property. Thirdly, experimental investigations on the exclusion zone formation near the surface of an ion exchange medium in the presence of a steady channel flow were discussed. The exclusion zone was formed by diffusive flux of ions transporting into the nanoporous membrane. Exchange of cations at the Nafion/liquid interface created the concentration gradient of the ions near the side walls, which then formed an exclusion zone of suspended particles. Different types of charged particles were tested to visualize exclusion zones under different conditions. Then the formation of exclusion zone in the channel flow was used as a method for water cleaning. Lastly, spatiotemporal concentration profile of diffusion-convection layer during ICP process had been directly measured with patterned Au microelectrode. Unlike

the traditional diffusion-convection layer which had linear concentration profile, the measured data showed near plateau concentration distribution over the diffusion-convection layer in a microfluidic environment. Even though, plateau concentration region had rather higher concentration ($\sim 0.6 c_0$) compare to ion depletion zone, it also acted as a distinct boundary to the movement of charged molecules as well.

Investigating concentration boundary layer is an important subject since the layer divides bulk concentration and altered concentration which is the starting point of new physical properties. For example, amplification of electric field, vortex formation due to high electro-osmotic flow, pH variation caused by ion concentration change and different movement of analyte arise at the concentration boundary layer. If we can properly obtain the concentration boundary layer profile, not only does it help exploring various unique phenomena arising from the permselective ion transportation but also it can support ground data when conceiving engineering applications. However, modeling electrokinetic transport phenomena requires simultaneous solution of continuity equation, Navier-Stokes equation, Nernst-Planck equation, Poisson equation and physical properties like device geometry, surface potential, porosity of the nanoporous membrane *etc.* Due to these diversity and complexity, answering the exact concentration boundary layer profiles is still an enigma. Experimental solutions are even more complex to acquire because direct measurement of concentration profiles is realistically unfeasible. So one needs to utilize variety of methods to acquire the concentration boundary layer. This thesis enlightened the role of concentration boundary layer where permselective ion transportation exists. Various experimental methods were adopted to elucidate the properties of concentration boundary layer in specific

conditions. In addition to the analytical approach based on experimental results, practical devices were conceived to solve engineering problems such as experimental conveniences, non-destructive cellular preconcentrator and water treatment. Moreover, sophisticated micro/nanofluidic phenomena had been characterized and discussed in this thesis. Given the importance of investigating concentration profile of boundary layer, we hope that this thesis would broaden the knowledge of the physical properties of ICP and diffusiophoresis.

Appendix

A. Pathogen preparation

Dr. Jina Yang who belongs to School of Chemical and Biological Engineering in Seoul National University provided the pathogens in chapter 4.

The Phusion polymerase, restriction enzymes, Quick ligase kit and pBR322 plasmid were purchased from New England Biolabs (Ipswich, MA, USA). The oligonucleotides, whose sequence was denoted in Appendix Table A.1, were synthesized by Bioneer (Daejeon, Korea). One Shot MachT1 (Invitrogen, Carlsbad, CA, USA) was used for standard cloning. All reagents for media preparation were purchased from BD Bioscience (Sparks, MD, USA) and ampicillin was obtained from Gold Biotech (St. Louis, MO, USA).

To visualize the bacterial cells, the cells were transformed with the plasmid harboring superfolder green fluorescent protein (sfGFP). The pG-OXB20-GFP plasmid expressing sfGFP under the control of strong constitutive promoter (OXB20) and synthetic 5'-untranslated region (5'-UTR) was used as a template to construct the pBR322-OXB20-GFP plasmid by the standard cloning procedure. The vector backbone was amplified from pBR322 with XbaI-pBR322-R and Bsu36I-pBR322-F primers. The OXB20-GFP was amplified from pGEM-OXB20-GFP with XbaI-OXB20-F and Bsu36I-GFP-R primers. These amplified fragments were digested by XbaI and Bsu36 and ligated by Quick ligase kit.

The pG-OXB20-GFP and pBR322-OXB20-GFP plasmids were introduced into *E. coli* W3110 (ATCC 27325) and *S. typhimurium* (ATCC 19585) by electroporation (2.5 kV, 200 Ω , 25 μ F in 0.2 cm-gap cuvette). The transformed *E. coli* W3110 and *S. typhimurium* were inoculated in 3 mL LB medium containing

ampicillin (50 µg/mL) to maintain plasmids and cultured at 37°C with 200 rpm. After overnight culture, cells were diluted in fresh media and additionally cultured for 12 hours. Matured cells were harvested by centrifugation and washed and resuspended in the sample solution.

B. Acid resistance assay for each pathogen

Dr. Jina Yang solely conducted acid resistance assay experiments for each pathogen in chapter 4.

Overnight cultures were diluted in fresh LB (Luria-Bertani) medium containing 50 mg/L ampicillin and incubated at 37 °C with shaking at 250 rpm for 2 hours. Cells were harvested and exposed to different acid solutions by resuspending cells in acidic 1mM NaCl adjusted with HCl. As untreated control, cells were also resuspended in 1 mM NaCl without adjustment. After 1 min static incubation at room temperature, cells were harvested and washed with 1mM NaCl. Cells than plated on the LB agar containing 50 mg/L ampicillin. After overnight incubation at 37 °C, viable cells were determined by counting colonies on the plates. Acid survivals were calculated by dividing CFU (colony forming unit) of acid treated cells by CFU of untreated controls.

Name	Sequence ^a
Bsu36I-pBR322-F	AAACCTCAGGTGAATGGAAGCCGGCGGCACCTC
XbaI-pBR322-R	ACTTCTAGACACGGTGCCTGACTGCGTTAG
XbaI-OXB20-F	CCCGTTAACTCTAGAAGCTGTTGTGACCGCTTG
Bsu36I-GFP-R	CACCTGAGGTTTCAGCAAAAACCCCTCAAGACC

^aUnderlined characters indicate enzyme sites for cloning.

Appendix Table A.1. Sequences of synthesized oligonucleotides.

C. Fully-coupled model for ion concentration boundary layer by ion exchange

Prof. Hyomin Lee who belongs to Department of Electrical and Computer Engineering in Seoul National University conducted fully coupled numerical simulation in Appendix C & D.

In our diffusion-convection problems, there were four species such as Na^+ , Cl^- , H^+ and OH^- in the electrolyte. The Nernst-Planck equations usually describe the mass conservation of each ionic species which are

$$\frac{\partial c_{Na}}{\partial t} = -\nabla \cdot \left(-D_{Na} \nabla c_{Na} - \frac{FD_{Na}}{RT} c_{Na} \nabla \psi + c_{Na} \mathbf{u} \right) \quad (\text{C.1})$$

$$\frac{\partial c_{Cl}}{\partial t} = -\nabla \cdot \left(-D_{Cl} \nabla c_{Cl} + \frac{FD_{Cl}}{RT} c_{Cl} \nabla \psi + c_{Cl} \mathbf{u} \right) \quad (\text{C.2})$$

$$\frac{\partial c_H}{\partial t} = -\nabla \cdot \left(-D_H \nabla c_H - \frac{FD_H}{RT} c_H \nabla \psi + c_H \mathbf{u} \right) + k_{rxn} (K_w - c_H c_{OH}) \quad (\text{C.3})$$

and

$$\frac{\partial c_{OH}}{\partial t} = -\nabla \cdot \left(-D_{OH} \nabla c_{OH} + \frac{FD_{OH}}{RT} c_{OH} \nabla \psi + c_{OH} \mathbf{u} \right) + k_{rxn} (K_w - c_H c_{OH}) \quad (\text{C.4})$$

where F is the Faraday constant, R is the gas constant, T is the absolute temperature, ψ is the electric potential, k_{rxn} is the reaction rate constant of spontaneous water ionization ($\text{H}^+ + \text{OH}^- \leftrightarrow \text{H}_2\text{O}$) and K_w is the equilibrium constant of the water ionization. Although the ion exchange cell was operated without any electrical power source, the term of the electro-migration (the second term of RHS in equation (C.1) – (C.3)) should be considered for describing the electric interactions to retain the local electroneutrality. The electroneutral interactions are expressed by the Poisson equation,

$$-\varepsilon \nabla^2 \psi = F(c_{Na} - c_{Cl} + c_H - c_{OH}) \quad (C.4)$$

Since the colloidal suspension was introduced by the external pressure, the imposed flow field was given by the Poiseuille flow in slit.

$$\mathbf{u} = \frac{3}{2} U_{mean} \left[1 - \left(\frac{x}{W} \right)^2 \right] \mathbf{e}_y \quad (C.5)$$

where U_{mean} is the mean velocity, x is the spatial coordinate of which origin is denoted in Figure 1(b), W is the half-width of the microchannel and \mathbf{e}_y is the unit vector of y -direction. In general, the externally imposed flow is stronger than another self-generated flow such as capillarity, diffusioosmosis[29, 72, 117, 118] or density variation driven flow[119-121]. So we only considered the externally imposed flow in equation (C.5). Notably, we could neglect the capillarity ion concentration polarization which is another mechanism to generate the natural ion depletion caused by the capillarity-induced convective flux as mentioned in our previous publications[68, 122] since we adopted cation-selective Nafion possessing low ability for absorbing water.

The boundary conditions at inlet were bulk concentrations for the Nernst-Planck equations ($c_{Na} = c_{Cl} = c_0$ and $c_H = c_{OH} = c_{H0}$ where c_0 and c_{H0} are the bulk concentration of each ionic species) and electrical ground for the Poisson equation ($\psi = 0$), respectively. At outlet, the outflow condition for Nernst-Planck equations (ionic flux through the boundary was composed of only convective flux) and electrical ground for the Poisson equation were imposed. At the typical microchannel walls, no penetration of ionic species for the Nernst-Planck equations and zero charge density for the Poisson equation were assigned. At the surface of nanoporous medium, the boundary conditions for equation (C.1), (C.2) and (C.4)

were the zero concentration of Na^+ and no penetration of Cl^- and OH^- , respectively as similar as Florea's model [71]. The condition of zero Na^+ concentration is guaranteed if the Donnan concentration of the nanoporous medium is higher than the bulk concentration. Since the 1:1 ion exchange occurred through the interface, the condition for equation (C.3) was

$$\mathbf{n} \cdot (\mathbf{j}_{\text{Na}} + \mathbf{j}_{\text{H}}) = 0 \quad (\text{C.7})$$

where \mathbf{n} is the outward normal vector, \mathbf{j}_{Na} and \mathbf{j}_{H} are the ionic fluxes of Na^+ and H^+ . The ionic flux of i -th species was expressed as

$$\mathbf{j}_i = -D_i \nabla c_i - \frac{z_i F D_i}{RT} c_i \nabla \psi + c_i \mathbf{u} \quad (\text{C.8})$$

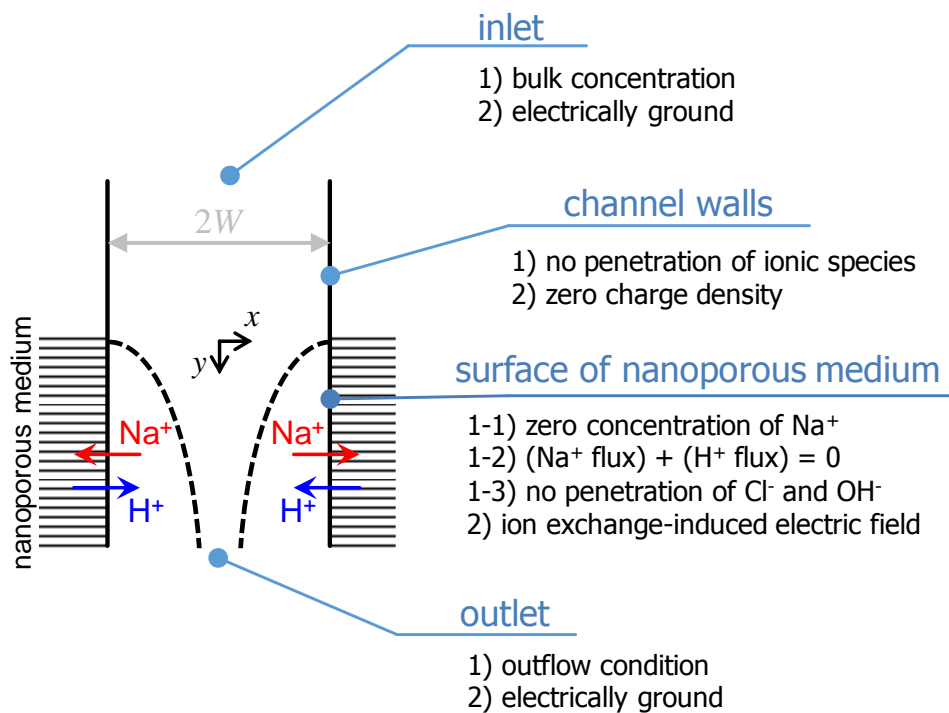
where subscript, i means the i -th species and z_i is the valence of i -th species. From the constraint of zero current density on the nanoporous medium (*i.e.* $\mathbf{n} \cdot (\mathbf{j}_{\text{Na}} - \mathbf{j}_{\text{Cl}} + \mathbf{j}_{\text{H}} - \mathbf{j}_{\text{OH}}) = 0$), we obtained the normal electric field at the interface as an electrical boundary condition for the Poisson equation as

$$-\mathbf{n} \cdot \nabla \psi = \frac{RT}{F} \frac{\mathbf{n} \cdot (D_{\text{Na}} \nabla c_{\text{Na}} - D_{\text{Cl}} \nabla c_{\text{Cl}} + D_{\text{H}} \nabla c_{\text{H}} - D_{\text{OH}} \nabla c_{\text{OH}})}{D_{\text{Na}} c_{\text{Na}} + D_{\text{Cl}} c_{\text{Cl}} + D_{\text{H}} c_{\text{H}} + D_{\text{OH}} c_{\text{OH}}} \quad (\text{C.9})$$

This was the ion exchange-induced electric field to retain the local electroneutrality.

D. Boundary conditions for 2D fully-coupled model.

Although we mentioned the boundary conditions for the 2D fully-coupled model to describe the ion concentration boundary layer in Appendix C, the summarized conditions presented for better understanding as shown in Appendix Figure D.1.



Appendix Figure D.1. Graphical representation of boundary conditions.

References

- [1] J. H. Masliyah and S. Bhattacharjee, *Electrokinetic and colloid transport phenomena*: John Wiley & Sons, 2006.
- [2] R. J. Hunter, *Zeta potential in colloid science: principles and applications* vol. 2: Academic press, 2013.
- [3] K. A. Mauritz and R. B. Moore, "State of understanding of Nafion," *Chemical reviews*, vol. 104, pp. 4535-4586, 2004.
- [4] J. Heo, H. J. Kwon, H. Jeon, B. Kim, S. J. Kim, and G. Lim, "Ultra-high-aspect-orthogonal and tunable three dimensional polymeric nanochannel stack array for BioMEMS applications," *Nanoscale*, vol. 6, pp. 9681-9688, 2014.
- [5] D. Deng, W. Aouad, W. A. Braff, S. Schlumpberger, M. E. Suss, and M. Z. Bazant, "Water purification by shock electrodialysis: Deionization, filtration, separation, and disinfection," *Desalination*, vol. 357, pp. 77-83, 2015.
- [6] B. Zaltzman and I. Rubinstein, "Electro-osmotic slip and electroconvective instability," *Journal of Fluid Mechanics*, vol. 579, pp. 173-226, 2007.
- [7] R. B. Schoch, J. Han, and P. Renaud, "Transport phenomena in nanofluidics," *Reviews of modern physics*, vol. 80, p. 839, 2008.
- [8] D. Stein, M. Kruthof, and C. Dekker, "Surface-charge-governed ion transport in nanofluidic channels," *Physical Review Letters*, vol. 93, p. 035901, 2004.
- [9] H. Cui, K. Horiuchi, P. Dutta, and C. F. Ivory, "Multistage isoelectric focusing in a polymeric microfluidic chip," *Analytical chemistry*, vol. 77, pp. 7878-7886, 2005.
- [10] D. J. Harrison, K. Fluri, K. Seiler, Z. Fan, C. S. Effenhauser, and A. Manz, "Micromachining a miniaturized capillary electrophoresis-based chemical analysis system on a chip," *Science*, vol. 261, pp. 895-897, 1993.
- [11] R. S. Foote, J. Khandurina, S. C. Jacobson, and J. M. Ramsey, "Preconcentration of proteins on microfluidic devices using porous silica membranes," *Analytical Chemistry*, vol. 77, pp. 57-63, 2005.
- [12] J. Lichtenberg, E. Verpoorte, and N. F. de Rooij, "Sample preconcentration by field amplification stacking for microchip-based capillary electrophoresis," *Electrophoresis*, vol. 22, pp. 258-271, 2001.
- [13] B. Jung, R. Bharadwaj, and J. G. Santiago, "On-chip millionfold sample stacking using transient isotachopheresis," *Analytical chemistry*, vol. 78, pp. 2319-2327, 2006.
- [14] R. D. Oleschuk, L. L. Shultz-Lockyear, Y. Ning, and D. J. Harrison, "Trapping of bead-based reagents within microfluidic systems: on-chip solid-phase extraction and electrochromatography," *Analytical chemistry*, vol. 72, pp. 585-590, 2000.
- [15] S. Song, A. K. Singh, and B. J. Kirby, "Electrophoretic concentration of proteins at laser-patterned nanoporous membranes in microchips," *Analytical Chemistry*, vol. 76, pp. 4589-4592, 2004.
- [16] R. F. Probstein, *Physicochemical hydrodynamics: an introduction*: John Wiley & Sons, 2005.
- [17] S. J. Kim, Y.-C. Wang, J. H. Lee, H. Jang, and J. Han, "Concentration polarization and nonlinear electrokinetic flow near a nanofluidic channel," *Physical review letters*, vol. 99, p. 044501, 2007.
- [18] T. Pundik, I. Rubinstein, and B. Zaltzman, "Bulk electroconvection in electrolyte," *Physical Review E*, vol. 72, p. 061502, 2005.
- [19] Y.-C. Wang, A. L. Stevens, and J. Han, "Million-fold preconcentration of proteins and peptides by nanofluidic filter," *Analytical chemistry*, vol. 77, pp. 4293-4299, 2005.
- [20] G. Yossifon and H.-C. Chang, "Selection of nonequilibrium overlimiting currents: universal depletion layer formation dynamics and vortex instability," *Physical review letters*, vol. 101, p. 254501, 2008.

- [21] S. Nam, I. Cho, J. Heo, G. Lim, M. Z. Bazant, D. J. Moon, *et al.*, "Experimental verification of overlimiting current by surface conduction and electro-osmotic flow in microchannels," *Physical review letters*, vol. 114, p. 114501, 2015.
- [22] S. J. Kim, L. D. Li, and J. Han, "Amplified electrokinetic response by concentration polarization near nanofluidic channel," *Langmuir*, vol. 25, pp. 7759-7765, 2009.
- [23] J.-m. Zheng and G. H. Pollack, "Long-range forces extending from polymer-gel surfaces," *Physical Review E*, vol. 68, p. 031408, 2003.
- [24] K. Green and T. Otori, "Direct measurements of membrane unstirred layers," *The Journal of physiology*, vol. 207, pp. 93-102, 1970.
- [25] B. Derjaguin and M. Golovanov, "On long-range forces of repulsion between biological cells," *Colloids and Surfaces*, vol. 10, pp. 77-84, 1984.
- [26] J.-m. Zheng, W.-C. Chin, E. Khijniak, E. Khijniak Jr, and G. H. Pollack, "Surfaces and interfacial water: evidence that hydrophilic surfaces have long-range impact," *Advances in colloid and interface science*, vol. 127, pp. 19-27, 2006.
- [27] J. L. Anderson, "Colloid transport by interfacial forces," *Annual review of fluid mechanics*, vol. 21, pp. 61-99, 1989.
- [28] T.-Y. Chiang and D. Velegol, "Multi-ion diffusiophoresis," *Journal of colloid and interface science*, vol. 424, pp. 120-123, 2014.
- [29] D. Velegol, A. Garg, R. Guha, A. Kar, and M. Kumar, "Origins of concentration gradients for diffusiophoresis," *Soft matter*, vol. 12, pp. 4686-4703, 2016.
- [30] S. H. Ko, Y.-A. Song, S. J. Kim, M. Kim, J. Han, and K. H. Kang, "Nanofluidic preconcentration device in a straight microchannel using ion concentration polarization," *Lab on a Chip*, vol. 12, pp. 4472-4482, 2012.
- [31] S. J. Kim, S. H. Ko, K. H. Kang, and J. Han, "Direct seawater desalination by ion concentration polarization," *Nature Nanotechnology*, vol. 5, p. 297, 2010.
- [32] H. Jeon, H. Lee, K. H. Kang, and G. Lim, "Ion concentration polarization-based continuous separation device using electrical repulsion in the depletion region," *Scientific reports*, vol. 3, p. 3483, 2013.
- [33] R. Kwak and J. Han, "Half-Cell Ion Concentration Polarization on Nafion-Coated Electrode," *The journal of physical chemistry letters*, 2018.
- [34] G. Yossifon, P. Mushenheim, Y.-C. Chang, and H.-C. Chang, "Nonlinear current-voltage characteristics of nanochannels," *Physical Review E*, vol. 79, p. 046305, 2009.
- [35] Q. Pu, J. Yun, H. Temkin, and S. Liu, "Ion-enrichment and ion-depletion effect of nanochannel structures," *Nano letters*, vol. 4, pp. 1099-1103, 2004.
- [36] P. N. Nge, C. I. Rogers, and A. T. Woolley, "Advances in microfluidic materials, functions, integration, and applications," *Chemical reviews*, vol. 113, pp. 2550-2583, 2013.
- [37] E. V. Dydek, B. Zaltzman, I. Rubinstein, D. Deng, A. Mani, and M. Z. Bazant, "Overlimiting current in a microchannel," *Physical review letters*, vol. 107, p. 118301, 2011.
- [38] I. Cho, W. Kim, J. Kim, H.-Y. Kim, H. Lee, and S. J. Kim, "Non-negligible Diffusio-osmosis inside an ion concentration polarization layer," *Physical review letters*, vol. 116, p. 254501, 2016.
- [39] I. Cho, G. Y. Sung, and S. J. Kim, "Overlimiting current through ion concentration polarization layer: hydrodynamic convection effects," *Nanoscale*, vol. 6, pp. 4620-4626, 2014.
- [40] S. Shin, O. Shardt, P. B. Warren, and H. A. Stone, "Membraneless water filtration using CO₂," *Nature Communications*, vol. 8, p. 15181, 2017.
- [41] J. Choi, K. Huh, D. J. Moon, H. Lee, S. Y. Son, K. Kim, *et al.*, "Selective preconcentration and online collection of charged molecules using ion concentration polarization," *RSC Advances*, vol. 5, pp. 66178-66184, 2015.
- [42] S. H. Ko, S. J. Kim, L. F. Cheow, L. D. Li, K. H. Kang, and J. Han, "Massively

- parallel concentration device for multiplexed immunoassays," *Lab on a Chip*, vol. 11, pp. 1351-1358, 2011.
- [43] L. F. Cheow and J. Han, "Continuous signal enhancement for sensitive aptamer affinity probe electrophoresis assay using electrokinetic concentration," *Analytical chemistry*, vol. 83, pp. 7086-7093, 2011.
- [44] H. Cho, H.-Y. Kim, J. Y. Kang, and T. S. Kim, "How the capillary burst microvalve works," *Journal of colloid and interface science*, vol. 306, pp. 379-385, 2007.
- [45] D. C. Duffy, J. C. McDonald, O. J. Schueller, and G. M. Whitesides, "Rapid prototyping of microfluidic systems in poly (dimethylsiloxane)," *Analytical chemistry*, vol. 70, pp. 4974-4984, 1998.
- [46] J. H. Lee, Y.-A. Song, and J. Han, "Multiplexed proteomic sample preconcentration device using surface-patterned ion-selective membrane," *Lab on a Chip*, vol. 8, pp. 596-601, 2008.
- [47] V. G. Levich, *Physicochemical hydrodynamics*: Prentice hall, 1962.
- [48] I. Rubinstein and L. Shtilman, "Voltage against current curves of cation exchange membranes," *Journal of the Chemical Society, Faraday Transactions 2: Molecular and Chemical Physics*, vol. 75, pp. 231-246, 1979.
- [49] S. M. Rubinstein, G. Manukyan, A. Staicu, I. Rubinstein, B. Zaltzman, R. G. Lammertink, *et al.*, "Direct observation of a nonequilibrium electro-osmotic instability," *Physical review letters*, vol. 101, p. 236101, 2008.
- [50] Y. Green and G. Yossifon, "Dynamical trapping of colloids at the stagnation points of electro-osmotic vortices of the second kind," *Physical Review E*, vol. 87, p. 033005, 2013.
- [51] B. D. Storey, B. Zaltzman, and I. Rubinstein, "Bulk electroconvective instability at high Peclet numbers," *Physical Review E*, vol. 76, p. 041501, 2007.
- [52] I. Rubinstein, B. Zaltzman, and I. Lerman, "Electroconvective instability in concentration polarization and nonequilibrium electro-osmotic slip," *Physical review E*, vol. 72, p. 011505, 2005.
- [53] K. Kim, W. Kim, H. Lee, and S. J. Kim, "Stabilization of ion concentration polarization layer using micro fin structure for high-throughput applications," *Nanoscale*, vol. 9, pp. 3466-3475, 2017.
- [54] B. Kim, R. Kwak, H. J. Kwon, V. S. Pham, M. Kim, B. Al-Anzi, *et al.*, "Purification of high salinity brine by multi-stage ion concentration polarization desalination," *Scientific reports*, vol. 6, p. 31850, 2016.
- [55] S. J. Kim, S. H. Ko, R. Kwak, J. D. Posner, K. H. Kang, and J. Han, "Multi-vortical flow inducing electrokinetic instability in ion concentration polarization layer," *Nanoscale*, vol. 4, pp. 7406-7410, 2012.
- [56] R. Kwak, G. Guan, W. K. Peng, and J. Han, "Microscale electro dialysis: Concentration profiling and vortex visualization," *Desalination*, vol. 308, pp. 138-146, 2013.
- [57] S. J. Kim, Y.-A. Song, and J. Han, "Nanofluidic concentration devices for biomolecules utilizing ion concentration polarization: theory, fabrication, and applications," *Chemical Society Reviews*, vol. 39, pp. 912-922, 2010.
- [58] B. Jung, R. Bharadwaj, and J. G. Santiago, "Thousandfold signal increase using field-amplified sample stacking for on-chip electrophoresis," *Electrophoresis*, vol. 24, pp. 3476-3483, 2003.
- [59] S. J. Kim and J. Han, "Self-sealed vertical polymeric nanoporous-junctions for high-throughput nanofluidic applications," *Analytical chemistry*, vol. 80, pp. 3507-3511, 2008.
- [60] R. Kwak, S. J. Kim, and J. Han, "Continuous-flow biomolecule and cell concentrator by ion concentration polarization," *Analytical chemistry*, vol. 83, pp. 7348-7355, 2011.
- [61] O. S. Andersen and R. E. Koeppe, "Bilayer thickness and membrane protein

- function: an energetic perspective," *Annu. Rev. Biophys. Biomol. Struct.*, vol. 36, pp. 107-130, 2007.
- [62] R. Paul, J. Apel, S. Klaus, F. Schügner, P. Schwindke, and H. Reul, "Shear stress related blood damage in laminar couette flow," *Artificial organs*, vol. 27, pp. 517-529, 2003.
- [63] L. Leverett, J. Hellums, C. Alfrey, and E. Lynch, "Red blood cell damage by shear stress," *Biophysical journal*, vol. 12, pp. 257-273, 1972.
- [64] S. Sutura and M. Mehrjardi, "Deformation and fragmentation of human red blood cells in turbulent shear flow," *Biophysical Journal*, vol. 15, pp. 1-10, 1975.
- [65] R. F. Ismagilov, A. Schwartz, N. Bowden, and G. M. Whitesides, "Autonomous Movement and Self-Assembly," *Angewandte Chemie*, vol. 114, pp. 674-676, 2002.
- [66] A. Céline, S. Fréour, F. Jacquemin, and P. Casari, "The hygroscopic behavior of plant fibers: a review," *Frontiers in chemistry*, vol. 1, p. 43, 2014.
- [67] J. Bae, J. Lee, S. Kim, J. Ha, B.-S. Lee, Y. Park, *et al.*, "Flutter-driven triboelectrification for harvesting wind energy," *Nature communications*, vol. 5, p. 4929, 2014.
- [68] S. Park, Y. Jung, S. Y. Son, I. Cho, Y. Cho, H. Lee, *et al.*, "Capillarity ion concentration polarization as spontaneous desalting mechanism," *Nature communications*, vol. 7, p. 11223, 2016.
- [69] S.-J. Park, M. Gazzola, K. S. Park, S. Park, V. Di Santo, E. L. Blevins, *et al.*, "Phototactic guidance of a tissue-engineered soft-robotic ray," *Science*, vol. 353, pp. 158-162, 2016.
- [70] A. S. Gladman, E. A. Matsumoto, R. G. Nuzzo, L. Mahadevan, and J. A. Lewis, "Biomimetic 4D printing," *Nature materials*, vol. 15, p. 413, 2016.
- [71] D. Florea, S. Musa, J. M. Huyghe, and H. M. Wyss, "Long-range repulsion of colloids driven by ion exchange and diffusiophoresis," *Proceedings of the National Academy of Sciences*, vol. 111, pp. 6554-6559, 2014.
- [72] R. Niu, P. Kreissl, A. T. Brown, G. Rempfer, D. Botin, C. Holm, *et al.*, "Microfluidic pumping by micromolar salt concentrations," *Soft matter*, vol. 13, pp. 1505-1518, 2017.
- [73] D. Prieve, J. Anderson, J. Ebel, and M. Lowell, "Motion of a particle generated by chemical gradients. Part 2. Electrolytes," *Journal of Fluid Mechanics*, vol. 148, pp. 247-269, 1984.
- [74] W. Wang, W. Duan, S. Ahmed, T. E. Mallouk, and A. Sen, "Small power: Autonomous nano-and micromotors propelled by self-generated gradients," *Nano Today*, vol. 8, pp. 531-554, 2013.
- [75] J. S. Paustian, R. N. Azevedo, S.-T. B. Lundin, M. J. Gilkey, and T. M. Squires, "Microfluidic microdialysis: Spatiotemporal control over solution microenvironments using integrated hydrogel membrane microwindows," *Physical Review X*, vol. 3, p. 041010, 2013.
- [76] A. Banerjee, I. Williams, R. N. Azevedo, M. E. Helgeson, and T. M. Squires, "Solutio-inertial phenomena: Designing long-range, long-lasting, surface-specific interactions in suspensions," *Proceedings of the National Academy of Sciences*, vol. 113, pp. 8612-8617, 2016.
- [77] B. Abécassis, C. Cottin-Bizonne, C. Ybert, A. Ajdari, and L. Bocquet, "Boosting migration of large particles by solute contrasts," *Nature materials*, vol. 7, p. 785, 2008.
- [78] N. Shi, R. Nery-Azevedo, A. I. Abdel-Fattah, and T. M. Squires, "Diffusiophoretic focusing of suspended colloids," *Physical review letters*, vol. 117, p. 258001, 2016.
- [79] S. Shin, J. T. Ault, J. Feng, P. B. Warren, and H. A. Stone, "Low-Cost Zeta Potentiometry Using Solute Gradients," *Advanced Materials*, vol. 29, 2017.
- [80] J. L. Moran and J. D. Posner, "Phoretic self-propulsion," *Annual Review of Fluid Mechanics*, vol. 49, pp. 511-540, 2017.
- [81] J.-m. Zheng, A. Wexler, and G. H. Pollack, "Effect of buffers on aqueous solute-

- exclusion zones around ion-exchange resins," *Journal of colloid and interface science*, vol. 332, pp. 511-514, 2009.
- [82] C. O'Rourke, I. Klyuzhin, J. S. Park, and G. H. Pollack, "Unexpected water flow through Nafion-tube punctures," *Physical Review E*, vol. 83, p. 056305, 2011.
- [83] C.-S. Chen, W.-J. Chung, I. C. Hsu, C.-M. Wu, and W.-C. Chin, "Force field measurements within the exclusion zone of water," *Journal of biological physics*, vol. 38, pp. 113-120, 2012.
- [84] R. Das and G. H. Pollack, "Charge-Based Forces at the Nafion–Water Interface," *Langmuir*, vol. 29, pp. 2651-2658, 2013.
- [85] I. N. Huszár, Z. Mártonfalvi, A. J. Laki, K. Iván, and M. Kellermayer, "Exclusion-zone dynamics explored with microfluidics and optical tweezers," *Entropy*, vol. 16, pp. 4322-4337, 2014.
- [86] S. Musa, D. Florea, H. M. Wyss, and J. M. Huyghe, "Convection associated with exclusion zone formation in colloidal suspensions," *Soft matter*, vol. 12, pp. 1127-1132, 2016.
- [87] I. Klyuzhin, A. Symonds, J. Magula, and G. H. Pollack, "New method of water purification based on the particle-exclusion phenomenon," *Environmental science & technology*, vol. 42, pp. 6160-6166, 2008.
- [88] B. Kim, J. Heo, H. J. Kwon, S. J. Cho, J. Han, S. J. Kim, *et al.*, "Tunable ionic transport for a triangular nanochannel in a polymeric nanofluidic system," *ACS nano*, vol. 7, pp. 740-747, 2012.
- [89] R. B. BIRD, W. E. STEWART, and E. N. LIGHTFOOT, "Transport Phenomena, 430," ed: John Wiley & Sons, New York, 2007.
- [90] D. H. Belhatche, "Choose appropriate wastewater treatment technologies," *Chemical engineering progress*, vol. 91, 1995.
- [91] M. N. Chong, B. Jin, C. W. Chow, and C. Saint, "Recent developments in photocatalytic water treatment technology: a review," *Water research*, vol. 44, pp. 2997-3027, 2010.
- [92] D. Di Carlo, D. Irimia, R. G. Tompkins, and M. Toner, "Continuous inertial focusing, ordering, and separation of particles in microchannels," *Proceedings of the National Academy of Sciences*, vol. 104, pp. 18892-18897, 2007.
- [93] D. Di Carlo, "Inertial microfluidics," *Lab on a Chip*, vol. 9, pp. 3038-3046, 2009.
- [94] S. H. Roelofs, B. Kim, J. C. Eijkel, J. Han, A. van den Berg, and M. Odijk, "Capacitive deionization on-chip as a method for microfluidic sample preparation," *Lab on a Chip*, vol. 15, pp. 1458-1464, 2015.
- [95] K. A. Soni, A. K. Balasubramanian, A. Beskok, and S. D. Pillai, "Zeta potential of selected bacteria in drinking water when dead, starved, or exposed to minimal and rich culture media," *Current microbiology*, vol. 56, pp. 93-97, 2008.
- [96] S. R. Waterman and P. Small, "Acid-sensitive enteric pathogens are protected from killing under extremely acidic conditions of pH 2.5 when they are inoculated onto certain solid food sources," *Applied and Environmental Microbiology*, vol. 64, pp. 3882-3886, 1998.
- [97] E. K. Bomati, J. E. Haley, J. P. Noel, and D. D. Deheyn, "Spectral and structural comparison between bright and dim green fluorescent proteins in *Amphioxus*," *Scientific reports*, vol. 4, p. 5469, 2014.
- [98] Y. Cheng and C. I. Moraru, "Long-range interactions keep bacterial cells from liquid-solid interfaces: Evidence of a bacteria exclusion zone near Nafion surfaces and possible implications for bacterial attachment," *Colloids and Surfaces B: Biointerfaces*, vol. 162, pp. 16-24, 2018.
- [99] B. J. Kirby, *Micro-and nanoscale fluid mechanics: transport in microfluidic devices*: Cambridge university press, 2010.
- [100] S. Y. Son, S. Lee, H. Lee, and S. J. Kim, "Engineered nanofluidic preconcentration devices by ion concentration polarization," *BioChip Journal*, vol. 10, pp. 251-261, 2016.

- [101] S. I. Han, Y. K. Yoo, J. Lee, C. Kim, K. Lee, T. H. Lee, *et al.*, "High-ionic-strength pre-concentration via ion concentration polarization for blood-based biofluids," *Sensors and Actuators B: Chemical*, vol. 268, pp. 485-493, 2018.
- [102] L. M. Fu, H. H. Hou, P. H. Chiu, and R. J. Yang, "Sample pre-concentration from dilute solutions on micro/nanofluidic platforms: A review," *Electrophoresis*, vol. 39, pp. 289-310, 2018.
- [103] H. Lee, J. Choi, E. Jeong, S. Baek, H. C. Kim, J.-H. Chae, *et al.*, "dCas9-mediated Nano-electrohydrodynamic Direct Detection of Target Gene for Liquid Biopsy," *Nano letters*, 2018.
- [104] I. Rubinstein and B. Zaltzman, "Electro-osmotically induced convection at a permselective membrane," *Physical Review E*, vol. 62, p. 2238, 2000.
- [105] S. Sohn, I. Cho, S. Kwon, H. Lee, and S. J. Kim, "Surface conduction in a microchannel," *Langmuir*, vol. 34, pp. 7916-7921, 2018.
- [106] S. I. Han, K. S. Hwang, R. Kwak, and J. H. Lee, "Microfluidic paper-based biomolecule preconcentrator based on ion concentration polarization," *Lab on a Chip*, vol. 16, pp. 2219-2227, 2016.
- [107] T. A. Zangle, A. Mani, and J. G. Santiago, "On the propagation of concentration polarization from microchannel–nanochannel interfaces Part II: numerical and experimental study," *Langmuir*, vol. 25, pp. 3909-3916, 2009.
- [108] F. C. Leinweber and U. Tallarek, "Nonequilibrium electrokinetic effects in beds of ion-permselective particles," *Langmuir*, vol. 20, pp. 11637-11648, 2004.
- [109] D. Milanova, R. D. Chambers, S. S. Bahga, and J. G. Santiago, "Electrophoretic mobility measurements of fluorescent dyes using on-chip capillary electrophoresis," *Electrophoresis*, vol. 32, pp. 3286-3294, 2011.
- [110] K. Horiuchi and P. Dutta, "Joule heating effects in electroosmotically driven microchannel flows," *International journal of heat and mass transfer*, vol. 47, pp. 3085-3095, 2004.
- [111] J. Kim, H.-Y. Kim, H. Lee, and S. J. Kim, "Pseudo 1-D Micro/Nanofluidic Device for Exact Electrokinetic Responses," *Langmuir*, vol. 32, pp. 6478-6485, 2016.
- [112] H. Lee, J. Kim, H. Kim, H.-Y. Kim, H. Lee, and S. J. Kim, "A concentration-independent micro/nanofluidic active diode using an asymmetric ion concentration polarization layer," *Nanoscale*, vol. 9, pp. 11871-11880, 2017.
- [113] R. Dhopeswarkar, D. Hlushkou, M. Nguyen, U. Tallarek, and R. M. Crooks, "Electrokinetics in microfluidic channels containing a floating electrode," *Journal of the American Chemical Society*, vol. 130, pp. 10480-10481, 2008.
- [114] S. E. Fosdick, K. N. Knust, K. Scida, and R. M. Crooks, "Bipolar electrochemistry," *Angewandte Chemie International Edition*, vol. 52, pp. 10438-10456, 2013.
- [115] S. Park and G. Yossifon, "Induced-charge electrokinetics, bipolar current, and concentration polarization in a microchannel–Nafion-membrane system," *Physical Review E*, vol. 93, p. 062614, 2016.
- [116] M. Z. Bazant and T. M. Squires, "Induced-charge electrokinetic phenomena: theory and microfluidic applications," *Physical Review Letters*, vol. 92, p. 066101, 2004.
- [117] J. J. McDermott, A. Kar, M. Daher, S. Klara, G. Wang, A. Sen, *et al.*, "Self-generated diffusioosmotic flows from calcium carbonate micropumps," *Langmuir*, vol. 28, pp. 15491-15497, 2012.
- [118] A. Kar, T.-Y. Chiang, I. Ortiz Rivera, A. Sen, and D. Velegol, "Enhanced transport into and out of dead-end pores," *ACS nano*, vol. 9, pp. 746-753, 2015.
- [119] S. Sengupta, D. Patra, I. Ortiz-Rivera, A. Agrawal, S. Shklyaev, K. K. Dey, *et al.*, "Self-powered enzyme micropumps," *Nature chemistry*, vol. 6, p. 415, 2014.
- [120] I. Ortiz-Rivera, H. Shum, A. Agrawal, A. Sen, and A. C. Balazs, "Convective flow reversal in self-powered enzyme micropumps," *Proceedings of the National Academy of Sciences*, vol. 113, pp. 2585-2590, 2016.

- [121] S. Das, O. E. Shklyae, A. Altemose, H. Shum, I. Ortiz-Rivera, L. Valdez, *et al.*, "Harnessing catalytic pumps for directional delivery of microparticles in microchambers," *Nature communications*, vol. 8, p. 14384, 2017.
- [122] Y. Oh, H. Lee, S. Y. Son, S. J. Kim, and P. Kim, "Capillarity ion concentration polarization for spontaneous biomolecular preconcentration mechanism," *Biomicrofluidics*, vol. 10, p. 014102, 2016.

초 록

본 논문은 선택적 이온전달 현상에 의해 유도된 농도경계층에 대해 실험을 통해 분석하고, 농도경계층의 물리적 특성들에 대하여 다룬 논문이다. 이때 농도경계층이란 마이크로채널과 나노채널이 인접해 있을 때 발생하는 원 농도와 농도가 달라지는 영역을 총괄하는 명칭으로써 해당 영역은 새로운 물리적 특성들이 발견되는 시작점이자 경계점이기에 그 연구가 중요한 의의를 지닌다. 만약 농도경계층 내의 농도분포를 정확히 알 수 있다면, 선택적 이온전달 현상에 의해 야기되는 고유한 물리적 현상들에 대한 이해도를 높일 수 있으며, 이를 활용하여 여러 공학적 응용처들에 적용 할 수 있다. 하지만 농도경계층의 농도분포와 관련한 해를 정확히 얻기란 쉽지 않다. 이는 미세유체역학의 지배방정식들이 복잡하게 얽혀있기 때문이다. 해를 구하기 위해서는 서로 얽혀 있는 연속 방정식, Navier-Stokes 방정식, Nernst-Planck equation 방정식, Poisson 방정식 등을 동시에 풀어야 하며, 경계조건들에 해당하는 소자들의 구조, 표면전위, 나노다공성 막의 공극률 등 또한 고려해야 한다. 이러한 복잡성들로 인해 농도경계층 내부의 농도 분포를 구하는 것은 아직 많은 부분들이 미지의 영역으로 남아있다. 추가적으로 실험적으로 시공간상의 농도분포를 정확히 측정하는 것은 사실상 불가능하며, 실험을 통해 농도분포를 얻는 과정 또한 매우 복잡하다.

본 논문은 선택적 이온전달에 대한 과학적 이해의 폭을 넓히기 위해

마이크로채널과 나노다공성 막이 결합되어 있는 소자에서 농도경계층의 역할 및 물리적 특성들에 대해 알아보았다. 농도경계층은 선택적 이온전달 현상에 의해 유도되며 그 메커니즘을 크게 2가지로 나눌 수 있다. 첫 번째는 전기이동에 의한 이온의 흐름이고, 두 번째는 확산이동에 의한 이온의 흐름이다. 따라서 주된 이온의 흐름이 각각일 때 나타나는 물리 현상인 이온농도분극 현상과 확산영동 현상을 중심으로 농도경계층을 분석하였다.

첫째로, 농도경계층의 분석을 용이하게 하기 위해 새로운 구조를 지니는 소자를 고안 하였다. 해당 소자는 액체/공기 소수성 표면에서 형성되는 가상의 밸브를 통해 가지 채널로 새는 액체를 제어 할 수 있는 특징을 지녔다. 해당 소자는 Young-Laplace 식을 활용한 소자로 기존에 100분에 달했던 실험 간 준비시간을 1-2분으로 대폭 줄일 수 있었다. 또한 제안한 소자가 채널 끝 단이 막혀있는 기존의 소자와 같은 물리적 특성을 보임을 이온농도분극의 확장, 전압 전류 곡선, 형광 물질의 움직임을 바탕으로 규명하였다.

둘째로, 네피온을 미세유체채널과 병렬 배치한 장치를 고안하여, 해당 장치에서 병렬 연결된 네피온이 농도경계층 형성에 어떠한 영향을 미치는 지를 확인하였다. 해당 소자는 앞 문단에서 고안한 구조를 소자에 적용하여 실험적 편리성과 함께 정확한 동전기적인 특성들을 얻을 수 있었다. 네피온은 양이온만을 투과시키는 나노다공성 막으로, 표면 패터닝 방식을 통해 마이크로채널과의 병렬 구조를 지닌 소자를 제작하였다. 그 결과, 제작된 소자는 기존 소자들에 비해 표면

전기전도도가 수십 배 늘어난 효과를 지녀 기존 소자들과 달리 농도경계층의 확장이 농도에 따라 시작지점이 달라짐을 확인 할 수 있었다. 해당 현상을 전기적 등가회로도룰 수립해 분석 및 해석을 진행하였다. 특히 제안한 소자의 독특한 특징은 고농도 전해질에서도 농도경계층 내부의 불안정한 전기대류성 와류가 억제된다는 점이 있었다. 기존 소자의 경우 고농도 전해질에서 불안정한 전기대류성 와류가 형성되어 생체시료의 농축에 어려움이 많았었지만, 제안한 소자를 활용할 경우 대상물질에 작용하는 힘인 전단응력을 최소화 하여 생체시료를 농축 할 수 있었다. 생체시료의 예로써 적혈구를 활용하여 비파괴적으로 생체시료를 농축/분리/회수 할 수 있음을 보였다.

셋째로, 확산영동이 이온의 흐름을 주도할 때 발생하는 농도경계층에 대한 연구를 수행하였다. 확산영동은 마이크로/나노 유체영역 내에서 일어나는 현상이기 때문에 직접적 관측의 어려움과 더불어 농도 차이가 있어야 한다는 특수한 조건 때문에 이와 관련한 연구가 많이 진행되지 못하였다. 본 논문에서는 선택적 이온전달의 확산방향과 유동의 방향이 수직인 2차원 시스템에서 확산에 의해 이온이 움직일 때 어떻게 농도경계층이 형성되는지에 대해 알아 보았다. 나노다공성 물질 주변에서의 이온 교환 및 입자 이동 현상을 셔우드 수라는 무차원 수로 표현을 하고, 다양한 셔우드 수에 대해 입자들이 밀리는 현상을 바탕으로 농도경계층을 분석 하였다. 또한 이온크로마토그래피 기계를 이용하여 실제 이온농도의 측정하고, 농도경계층을 수치화 할 수 있었다. 또한 이를 활용해 자발적 담수층을 형성하는 마이크로/나노 소자를

제작하였다.

마지막으로 이온농도분극 현상에 의해 발생하는 확산-대류 층의 시공간상의 농도분포가 직접적으로 측정되었다. 반도체 공정을 통해 제작한 금 미세전극들을 활용하여 미세유체채널 내의 부분 전위를 측정할 수 있었다. 기존의 확산-대류 층이 선형의 농도분포를 지니고 있었다며, 측정한 데이터를 바탕으로 마이크로채널 환경에서 확산-대류층 내부에 농도가 일정한 영역이 존재함을 확인하였다. 또한 일정 농도를 지닌 영역의 경우 기존의 이온공핍층에 비해 상대적으로 꽤 높은 농도를 지녔지만, 그럼에도 불구하고 물리적 특성을 나눌 수 있는 층으로써 역할을 수행함을 확인하였다.

본 논문에서는 다양한 실험적 방법들을 활용해서 특수한 조건하에서 농도경계층의 형성이 어떠한 새로운 물리적 특성들을 보이는지 살펴보았다. 크게 2가지 파트로 나누어 전기이동에 의해 형성되는 이온농도분극 현상에서의 농도경계층의 특성들(2,3,5장)과, 확산이동에 의해 형성되는 확산영동 현상에서의 농도경계층의 특성들(4장)에 대해 살펴보았다. 실험적 결과를 바탕으로, 물리적인 해석과 함께 농도경계층의 특성들을 분석하였으며, 특성들을 활용한 공학적 응용처들을 제시하였다. 본 논문을 통해 선택적 이온전달 현상에 의해 유도되는 농도경계층에 대한 이해도가 넓어지기를 바란다.

Key words: 마이크로/나노 유체역학, 선택적 이온전달, 이온농도분극 현상, 확산영동, 마이크로/나노 입자 농축 장치

Student number: 2014-22550